Pure Appl. Chem., Vol. 81, No. 10, pp. 1799–1828, 2009.
doi:10.1351/PAC-CON-08-09-24

Force field for the atomistic simulation of the properties of hydrazine, organic hydrazine derivatives, and energetic hydrazinium ionic liquids*

Keith E. Gutowski, Burcu Gurkan, and Edward J. Maginn‡

Department of Chemical and Biomolecular Engineering, University of Notre Dame, 182 Fitzpatrick Hall, Notre Dame, IN 46556-5637, USA

Abstract: A force field (FF) is reported for hydrazine (N_2H_4) and organic hydrazine derivatives, including monomethylhydrazine, 1,1-dimethylhydrazine, monoethylhydrazine, and 2-hydroxyethylhydrazine. The FF successfully reproduces a range of equilibrium properties, including vapor–liquid coexistence densities, vapor pressures, enthalpies of vaporization, and critical properties. Several dynamic properties, including self-diffusion coefficients and rotational time constants, are reported and found to be qualitatively consistent with experimental viscosities. Using this as a basis, a FF is also developed for the protonated forms of these species, i.e., hydrazinium-based cations. Properties of 1:1 energetic salts formed by pairing these cations with the nitrate anion are computed and compared with a limited amount of experimental data. The simulations indicate that the ionic liquid (IL) 2-hydroxyethylhydrazinum nitrate (2-HEHN) has significantly slower dynamics than the other hydrazinium ILs.

Keywords: energetic compounds; force field; hydrazine; hydrazinium; ionic liquids; molecular simulation.

INTRODUCTION

Hydrazine (N_2H_4) and its organic derivatives ($N_2R_1R_2R_3R_4$, R=H, organic) are very versatile chemical reagents for a variety of applications due to their extreme reactivity. Hydrazine itself is a highly reactive base and reducing agent. These applications are diverse in number and type, ranging from rocket propellants and explosives to military fuel cells, polymers (urethane polymerization), metal finishing (nickel plating), boiler water-feed deoxygenation, pesticides, and pharmaceuticals. The preparation, properties, and applications of hydrazine and its derivatives have been thoroughly summarized in a comprehensive work by E. W. Schmidt [1]. Historically, hydrazines and hydrazine mixtures have found the most widespread use as monopropellants and bipropellants in thrusters for rockets, satellites, and spacecraft. Hydrazine and hydrazine derivatives owe their energetic nature to the exothermicity of formation of the very stable nitrogen–nitrogen triple bond. The gas-phase combustion of hydrazine results in an enthalpy change of –622.08 kJ/mol [2].

Use of hydrazine as a monopropellant requires a catalyst that facilitates hydrazine decomposition. Spontaneous noble metal catalysts (typically immobilized on a solid support) that initiate hydrazine de-

*Paper based on a presentation at the 20th International Conference on Chemical Thermodynamics (ICCT 20), 3–8 August 2008, Warsaw, Poland. Other presentations are published in this issue, pp. 1719–1959.

‡Corresponding author: E-mail: ed@nd.edu

composition instantly and repeatedly have allowed for the development of simple and reliable monopropellant hydrazine systems. Organic hydrazine derivatives such as monomethylhydrazine (MMH) or 1,1-dimethylhydrazine (unsymmetrical dimethylhydrazine, UDMH) are not commonly used in practical monopropellant systems due to difficulties encountered with carbon deposition and subsequent catalyst poisoning or deactivation. MMH and UDMH are more routinely used in bipropellant applications, where the hydrazines are mixed with oxidants that result in reaction upon contact. Thus, these systems are deemed hypergolic and do not require external ignition devices. Hypergolic additives for hydrazine systems include dinitrogen tetroxide (N_2O_4), fuming nitric acid, hydrogen peroxide, or fluorine. These mixtures have been used in liquid rocket engines, most notably during the Apollo lunar missions, where engines must be restarted frequently and the fuel can be stored as liquids at room temperature [1].

Although widely used in the space program, hydrazine and organic hydrazine derivatives exhibit many properties that may deem their routine use in more common applications undesirable. The Environmental Protection Agency (EPA) has classified hydrazine as a Group B2, probable human carcinogen, while MMH and UDMH have not been classified [3]. However, MMH has been classified by the European Union directive as carcinogenic (category 2) to humans [4], and UDMH has been classified by the International Agency for Research Cancer (IARC) as possibly carcinogenic to humans [5]. Acute symptoms in humans from exposure (inhalation or contact) to hydrazine, MMH, and UDMH include eye, nose, and throat irritation and corrosion (burns), headache, nausea, and vomiting, and can lead to both acute and chronic kidney, liver, respiratory, and central nervous system damage. In addition to the carcinogenic and toxic effects of these compounds, hydrazines are also volatile, flammable, and very reactive [1].

The real and perceived hazards associated with the use of hydrazine and hydrazine derivatives have created a global initiative to develop less hazardous replacements within the propellant industry. Such concerns reached the headlines recently when the United States shot down a disabled satellite out of fears that hydrazine would be spread upon re-entry over populated areas [6]. Current safety regulations require considerable investment in equipment and handling procedures associated with fueling hydrazine-based propulsion systems. New monopropellants and bipropellants are desired with equivalent or superior performance, yet are less toxic and hazardous, safer to work with, and have less environmental impact (i.e., more "green") [7]. Several existing alternatives include hydroxylammonium nitrate (HAN) and hydrogen peroxide (H_2O_2), yet their adoption has lagged due to their uncertain track record of effectiveness and reliability.

Energetic salts, including the ammonium type, have long been considered as alternatives to molecular energetic compounds. Recently, considerable attention has been paid to classes of low-melting energetic salts, known collectively as ionic liquids (ILs). ILs are typically classified as salts formed by pairing an organic cation with an inorganic anion that, together, melt at or below 100 °C. As propellant candidates, ILs offer many inherent physical properties that are desired for new materials, including low melting points, high densities, negligible vapor pressures, and high thermal stabilities. Hydrazinium salts and ILs, derived from hydrazine and organic hydrazine derivatives, are particularly desirable as the chemistry associated with the cation has a long and rich history within the aerospace field. One set of hydrazinium salts that are suitable candidates for propellant applications was demonstrated experimentally [8] to be those formed from 2-hydroxyethylhydrazine (2-HEH) (see accompanying figure).

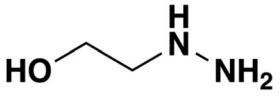

The 1:1 salts of 2-HEH have negligible vapor pressures, low melting points (<25 °C), high liquid densities, and, when formulated properly, can outperform hydrazine as a monopropellant. Additionally, 1:2 salts of 2-hydroxyhydrazine are typically solids and have even higher densities. Also, certain

2-hydroxyhydrazinium salts burn cleanly [8]. Considerable opportunities still exist to experimentally study these new classes of materials as propellant alternatives.

Due to inherent hazards associated with working with energetic materials, particularly hydrazine-based systems, computational methods and simulations are attractive alternatives or complements to experiments in elucidating physical properties. Although much is known about N_2H_4 and some other simple derivatives (MMH and UDMH), publicly available physical data is often deficient for mixtures, particularly those that are unstable or hypergolic, or more complex compounds. Interestingly, instances of classical simulations, both those based on molecular dynamics (MD) or Monte Carlo (MC) approaches, of hydrazine and its derivatives in the liquid state are uncommon in the scientific literature. This is unusual as these approaches are useful for understanding properties that are difficult to measure, i.e., those at extreme temperature or pressure. Furthermore, the design and estimation of the physical properties of new systems or compositions, such as hydrazinium-based ILs, is possible. Considerable attention has been paid to gas-phase studies of single molecules or clusters of hydrazine and organic hydrazines using ab initio (AI) electronic structure calculations [9]. Owing to the different conformations that are possible in hydrazine and the potential for extensive hydrogen bonding, gas-phase studies have been performed to better understand the nature of bonding in the molecule and the hydrogen-bonded clusters. Furthermore, conformational diversity of the organic derivatives has also been probed using these methods. For classical MD and MC simulations, AI studies of single molecules are critical for elucidation of intra- and intermolecular classical force field (FF) parameters. Very little information is available on these parameters for the hydrazine systems.

This paper reports the development of an internally consistent set of transferable FF parameters for hydrazine, some simple organic hydrazine derivatives, and 1:1 hydrazinium salts. Parameter assignment is based on AI electronic structure calculations at the density functional theory (DFT) level for all intramolecular parameters, and for intermolecular atomic charges. Intermolecular Lennard–Jones (LJ) parameters have been refined based on comparisons to available experimental data. These FF parameters were then used to calculate important thermodynamic and dynamic properties, including liquid densities, heats of vaporization, vapor–liquid coexistence curves, vapor pressures, heat capacities, self-diffusion coefficients, and rotational relaxation times for the following model systems: hydrazine (N_2H_4), MMH, UDMH, ethylhydrazine (MEH), and 2-HEH. The validated hydrazine FF parameters were extended to study the more complex 1:1 hydrazinium-based nitrate salts and ILs that are important for developing safer replacements or alternatives for current propellants.

FORCE FIELD DEVELOPMENT

The extent to which a classical molecular simulation accurately predicts thermophysical properties depends on the quality of the FF used to model the interactions in the fluid. Here, we have used a standard molecular mechanics FF, with the functional form

$$U^{\mathrm{tot}} = \sum_{\mathrm{bonds}} k_b (r - r_0)^2 + \sum_{\mathrm{angles}} k_\theta (\theta - \theta_0)^2 + \sum_{\mathrm{dihedrals}} k_\chi [1 + \cos(n\chi - \delta)] + \sum_{\mathrm{impropers}} k_\psi (\psi - \psi_0)^2 + \sum_{i=1}^{N-1} \sum_{j>i}^{N} \left\{ 4\varepsilon_{ij} \left[\left(\frac{\sigma_{ij}}{r_{ij}} \right)^{12} - \left(\frac{\sigma_{ij}}{r_{ij}} \right)^{6} \right] + \frac{q_i q_j}{4\pi\varepsilon_0 r_{ij}} \right\} \quad (1)$$

where the first four terms denote the intramolecular contributions and the remaining term denotes the intermolecular contributions to the total system energy, U^{tot}, respectively. The intramolecular terms for bond stretching and proper and improper angle bending are described by harmonic potentials with force constants k_b, k_θ, and k_ψ and nominal values of r_0, θ_0, and ψ_0. The dihedral motion is described by a Fourier cosine series where χ is the dihedral angle and the remaining parameters are fit to reproduce the

torsional energy curve, typically obtained from AI electronic structure calculations. The intermolecular potential is comprised of LJ and Coulombic energy terms. The LJ part is described by a 12-6 potential, with constants ε_{ij}, the depth of the potential well, and σ, the distance at which the interparticle potential is zero. The Lorentz–Berthelot combining rule is used for unlike atom parameters. The Coulombic part is modeled using fixed partial charges, q_i and q_j, on each atom center.

The Gaussian 03 suite of programs [10] was used to perform gas-phase minimizations of hydrazine, MMH, UDMH, MEH, and 2-HEH at the B3LYP/TZVP level [11]. This level of theory was found to accurately predict equilibrium structures compared to available experimental gas-phase results for these and related compounds. All optimized structures were characterized as having no imaginary frequencies, indicating that they are at least local minima on their respective potential energy surfaces. Every effort, however, was made to locate global minima. The nominal bond distances (r_0) and angles (θ_0) used in the current FF were determined from the minimized structures. The bond stretching force constants (k_b) were taken directly from the force constant matrix in internal coordinates and scaled [12]. This approach yields reliable force constants consistent with other FFs (i.e., CHARMM and Amber), as the k_b values are to a large extent decoupled from other internal coordinates, indicated by small off-diagonal elements in the force constant matrix. The same is not true for the angle bending force constants (k_θ), which are often strongly coupled with other internal coordinates, i.e., other bending or torsional modes, and thus cannot be directly taken from the force constant matrix. Unique k_θ values were derived by performing structural perturbations and single-point energy calculations corresponding to the angle of interest, coupled with appropriate scaling. The k_θ values were then averaged, assuming a harmonic approximation. FF parameters for bonds and angles of the hydrazines are reported in Tables 3 to 6. The parameters are grouped into various tables for clarity and readability.

A static point charge model is used in the description of Coulombic interactions, where partial charges are placed at the atomic sites. Since partial charges are not quantum mechanical (QM) observables, several approaches have been developed to assign them. Here, the CHELPG procedure [13] has been chosen, consistent with previous FF philosophies [14]. In the CHELPG procedure, the electrostatic potential is projected onto the atoms in a molecule, such that the gas-phase dipole moment is conserved. The electron density used for the CHELPG analysis has been calculated at the B3LYP/TZVP level. LJ parameters were initially assigned using parameters from the literature [15], and refined to reproduce experimental thermophysical data described in the Results and Discussion section. In particular, the N and H LJ parameters of N_2H_4 were adjusted to reproduce the experimental liquid densities and heats of vaporization at different temperatures. For the remaining compounds, the LJ parameters (excluding NH2, HA, and HB) were taken from the CHARMM FF [15] and were found to adequately reproduce experimental liquid densities and heats of vaporization. The partial charges were calculated for the optimized structures and kept constant during the dihedral analysis described hereafter. Partial charges and LJ parameters for each hydrazine molecule are listed in Tables 1 and 2, along with corresponding atom label and atom type. Atom labels associated with each molecule are shown in Fig. 1.

Table 1 Partial atomic charges (CHELPG at B3LYP/TZVP level) and atom types for molecular N_2H_4, MMH, UDMH, MEH, and 2-HEH.

N_2H_4			MMH			UDMH		
Atom	Type	q_i(e)	Atom	Type	q_i(e)	Atom	Type	q_i(e)
N1	NH2	–0.6705	N1	NH2	–0.7778	N1	NH2	–0.7281
H2	HA	0.3468	H2	HA	0.3755	H2	HA	0.3517
H3	HB	0.3237	H3	HB	0.3445	H3	HB	0.3517
N4	NH2	–0.6705	N4	NH2	–0.4739	N4	NH2	–0.3225
H5	HA	0.3468	H5	HA	0.3594	C5	CT3A	–0.0364
H6	HB	0.3237	C6	CT3	0.1522	C6	CT3B	–0.0364
			H7–H9	HA3	0.0067	H7–H9	HA3	0.0700
						H10–H12	HA3	0.0700

MEH			2-HEH		
Atom	Type	q_i(e)	Atom	Type	q_i(e)
N1	NH2	–0.7468	N1	NH2	–0.7573
H2	HA	0.3629	H2	HA	0.3700
H3	HB	0.3193	H3	HB	0.3290
N4	NH2	–0.5030	N4	NH2	–0.4711
H5	HA	0.3532	H5	HA	0.3644
C6	CT2	0.3520	C6	CT2	0.2069
C7	CT3	–0.3036	C7	CT2	0.1934
H8	HA2	–0.0049	H8	HA2	–0.0041
H9	HA2	–0.0346	H9	HA2	0.0280
H10–H12	HA3	0.0685	H10	HA2	–0.0078
			H11	HA2	0.0008
			O12	OH1	–0.6675
			H13	HO1	0.4153

Table 2 LJ parameters for corresponding atom types in molecular N_2H_4, MMH, UDMH, MEH, and 2-HEH.

Type	σ (Å)	ε_i (kJ mol^{-1})
NH2	3.368	0.711 28
HA	1.559	0.065 69
HB	1.559	0.065 69
CT2	4.009	0.334 72
CT3[a]	4.009	0.334 72
HA2	2.388	0.117 15
HA3	2.388	0.117 15
OH1	3.029	0.636 39
HO1	0.400	0.192 46

[a]CT3, CT3A, and CT3B.

Table 3 Bond, angle, and dihedral FF parameters for N_2H_4.

Bond	Force constant k_b (kJ mol^{-1} Å^{-2})	r_0 (Å)	Angle	Force constant k_θ (kJ mol^{-1} rad^{-2})	θ_0 (deg)
NH2-HA	1882.80	1.013	HA-NH2-NH2	271.96	107.63
NH2-HB	1882.80	1.017	HB-NH2-NH2	271.96	112.32
NH2-NH2	1506.24	1.439	HA-NH2-HB	188.28	108.28
Dihedral	**Force constant k_χ (kJ mol^{-1})**	**n**	**δ**		
HA-NH2-NH2-HB	2.971 06	1	0.0		
	–6.334 99	2	180.0		
	1.640 13	3	0.0		
HA-NH2-NH2-HA	0.0000	3	0.0		
HB-NH2-NH2-HB	0.0000	3	0.0		

Table 4 Bond, angle, and dihedral FF parameters for MMH and MEH.

Bond	Force constant k_b (kJ mol^{-1} Å^{-2})	r_0 (Å)	Angle	Force constant k_θ (kJ mol^{-1} rad^{-2})	θ_0 (deg)
NH2-HA	1882.80	1.015	HA-NH2-NH2	271.96	107.63
NH2-HB	1882.80	1.023	HB-NH2-NH2	271.96	112.32
NH2-NH2	1506.24	1.433	HA-NH2-HB	188.28	108.28
NH2-CT2	1338.88	1.464	CT2- NH2-NH2	355.64	114.50
NH2-CT3	1380.72	1.460	CT3-NH2-NH2	355.64	114.38
CT2-CT3	1263.57	1.521	HA-NH2-CT2	209.20	109.59
CT2-HA2	1347.25	1.100	HA-NH2-CT3	209.20	110.51
CT3-HA3	1393.27	1.094	HA2-CT2-NH2	230.12	110.34
			HA3-CT3-NH2	230.12	110.34
			NH2-CT2-CT3	292.88	110.76
			HA2-CT2-CT3	188.28	109.86
			HA3-CT3-CT2	188.28	110.87
			HA2-CT2-HA2	146.44	107.54
			HA3-CT2-HA3	146.44	108.12

Dihedral	Force constant k_χ (kJ mol^{-1})	n	δ	Dihedral	Force constant k_χ (kJ mol^{-1})	n	δ
HA-NH2-NH2-HB	2.971 06	1	0.0	HA-NH2-CT2-HA2	0.656 05	3	0.0
	–6.334 99	2	180.0	HA-NH2-CT3-HA3	0.656 05	3	0.0
	1.640 13	3	0.0	NH2-NH2-CT2-HA2	1.792 43	3	0.0
HA-NH2-NH2-CT2	3.942 16	1	0.0	NH2-NH2-CT3-HA3	1.792 43	3	0.0
	–6.107 38	2	180.0	HA-NH2-CT2-CT3	–0.233 89	1	0.0
	2.302 04	3	0.0		–0.192 46	2	180.0
	0.907 09	4	180.0		0.792 87	3	0.0
HA-NH2-NH2-CT3	3.942 16	1	0.0	NH2-NH2-CT2-CT3	3.725 85	1	0.0
	–6.107 38	2	180.0		1.196 21	2	180.0
	2.302 04	3	0.0		0.228 86	3	0.0
	0.907 09	4	180.0	HA-CT2-CT3-HA3	0.603 33	3	0.0
HA-NH2-NH2-HA	0.000 00	1	0.0	NH2-CT2-CT3-HA3	0.536 81	3	0.0
HB-NH2-NH2-CT2	0.000 00	1	0.0				
HB-NH2-NH2-CT3	0.000 00	1	0.0				

Table 5 Bond, angle, and dihedral FF parameters for UDMH.

Bond	Force constant k_b (kJ mol^{-1} Å^{-2})	r_0 (Å)	Angles	Force constant k_θ (kJ mol^{-1} rad^{-2})	θ_0 (deg)
NH2-HA	1882.80	1.015	HA-NH2-NH2	271.96	107.63
NH2-HB	1882.80	1.023	HB-NH2-NH2	271.96	112.32
NH2-NH2	1506.24	1.433	HA-NH2-HB	188.28	108.28
NH2-CT3A	1380.72	1.460	NH2-NH2-CT3A	355.64	108.73
NH2-CT3B	1380.72	1.460	NH2-NH2-CT3B	355.64	112.48
CT3A-HA3	1393.27	1.094	CT3A-NH2-CT3B	322.17	112.12
CT3B-HA3	1393.27	1.094	HA3-CT3A-NH2	230.12	110.34
			HA3-CT3B-NH2	230.12	110.34
			HA3-CT3A-HA3	146.44	108.12
			HA3-CT3B-HA3	146.44	108.12

Dihedral	Force constant k_χ (kJ mol^{-1})	n	δ	Dihedral	Force constant k_χ (kJ mol^{-1})	n	δ
HA-NH2-NH2-CT3B	3.942 16	1	0.0	HA3-CT3A-NH2-NH2	1.792 43	3	0.0
	–6.107 38	2	180.0	HA3-CT3B-NH2-NH2	1.792 43	3	0.0
	2.302 04	3	0.0	HA3-CT3A-NT-CT3B	0.679 48	3	0.0
	0.907 09	4	180.0	HA3-CT3B-NT-CT3A	0.679 48	3	0.0
HB-NH2-NH2-CT3A	3.942 16	1	0.0				
	–6.107 38	2	180.0				
	2.302 04	3	0.0				
	0.907 09	4	180.0				
HA-NH2-NH2-CT3A	0.000 00	1	0.0				
HB-NH2-NH2-CT3B	0.000 00	1	0.0				

Table 6 Bond, angle, and dihedral FF parameters for 2-HEH.

Bond	Force constant k_b (kJ mol^{-1} Å^{-2})	r_0 (Å)	Angle	Force constant k_θ (kJ mol^{-1} rad^{-2})	θ_0 (deg)
NH2-HA	1882.80	1.015	HA-NH2-NH2	271.96	107.63
NH2-HB	1882.80	1.023	HB-NH2-NH2	271.96	112.32
NH2-NH2	1506.24	1.433	HA-NH2-HB	188.28	108.28
NH2-CT2	1338.88	1.464	HA-NH2-CT2	209.20	109.59
CT2-CT2	1276.12	1.517	CT2-NH2-NH2	355.64	114.50
CT2-HA2	1347.25	1.100	HA2-CT2-NH2	230.12	110.34
OH1-CT2	1422.56	1.437	CT2-CT2-NH2	292.88	110.57
HO1-OH1	2217.52	0.964	HA2-CT2-CT2	188.28	109.13
			HA2-CT2-HA2	146.44	107.54
			OH1-CT2-CT2	251.04	110.61
			OH1-CT2-HA2	334.72	107.78
			HO1-OH1-CT2	217.57	109.07

Dihedral	Force constant k_χ (kJ mol^{-1})	n	δ	Dihedral	Force constant k_χ (kJ mol^{-1})	n	δ
HA-NH2-NH2-HB	2.971 06	1	0.0	NH2-NH2-CT2-CT2	3.725 85	1	0.0
	–6.334 99	2	180.0		1.196 21	2	180.0
	1.640 13	3	0.0		0.228 86	3	0.0

(*continues on next page*)

Table 6 (*Continued*).

Dihedral	Force constant k_χ (kJ mol^{-1})	n	δ	Dihedral	Force constant k_χ (kJ mol^{-1})	n	δ
HA-NH2-NH2-CT2	3.942 16	1	0.0	HA2-CT2-CT2-HA2	0.603 33	3	0.0
	–6.107 38	2	180.0	HA2-CT2-CT2-NH2	0.536 81	3	0.0
	2.302 04	3	0.0	OH1-CT2-CT2-HA2	0.809 19	3	0.0
	0.907 09	4	180.0	OH1-CT2-CT2-NH2	13.660 34	1	0.0
HA-NH2-NH2-HA	0.000 00	1	0.0		–4.241 74	2	180.0
HB-NH2-NH2-CT2	0.000 00	1	0.0		0.399 99	3	0.0
HA-NH2-CT2-HA2	0.656 47	3	0.0	HO1-OH1-CT2-HA2	0.746 84	3	0.0
NH2-NH2-CT2-HA2	1.792 43	3	0.0	HO1-OH1-CT2-CT2	–2.709 56	1	0.0
HA-NH2-CT2-CT2	–0.233 89	1	0.0		0.186 19	2	180.0
	–0.192 46	2	180.0		0.910 86	3	0.0
	0.792 87	3	0.0				

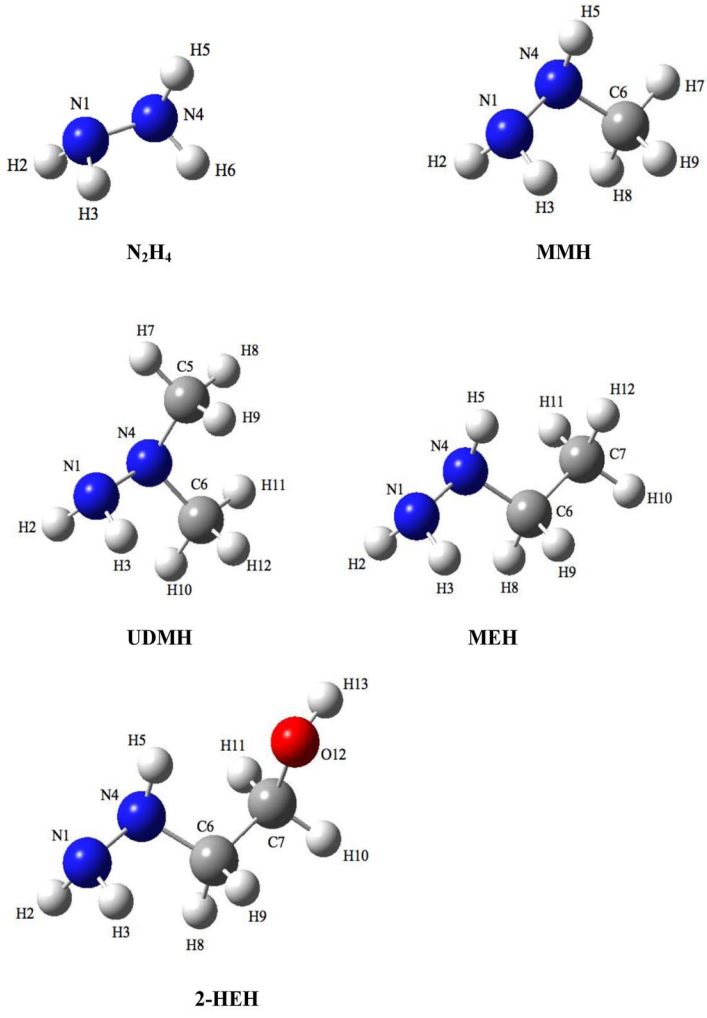

Fig. 1 Structures of N_2H_4, MMH, UDMH, MEH, and 2-HEH (optimized at B3LYP/TZVP level) and corresponding atom labels.

The dihedral analysis was performed using a procedure analogous to what has been described previously by Padua and Canongia Lopes [16]. Dihedral angle energy profiles were obtained by incrementally rotating (±10º) the angle under consideration through 180 or 360º, depending on the symmetry of the molecule. The approach entails a building-up procedure such that all unique combinations for a given central bond are assigned based on dihedral analysis of smaller molecules with similar chemical structures. Geometry optimizations were performed at each step at the B3LYP/TZVP level of theory, allowing the entire molecule to relax except the dihedral under study. Additional constraints on intramolecular degrees of freedom were added when necessary to obtain an energetic profile representative of the dihedral angle under investigation. The B3LYP/TZVP energy profile was found to closely reproduce MP2/cc-pVTZ(-f) results for these small molecules. Since nonbonded interactions can contribute significantly to the molecular mechanics (MM) dihedral energy profile, relaxed MM calculations were performed at each step during the dihedral scan with the particular FF dihedral parameters set to zero. The MM energies were then subtracted from the AI energies to obtain energy contributions solely from the dihedral rotation. This profile was then fit using a cosine series, as in eq. 1.

A dihedral angle of critical importance in hydrazine is the angle described by rotation about the N–N bond. Each nitrogen atom has a lone pair of electrons, thus making lone-pair:lone-pair and lone-pair:atom interactions critical. Figure 2 shows the H–N–N–H dihedral angle energy profile for N_2H_4. The potential shown is symmetric about the origin. The profile is characterized by two maxima, with barrier heights of ~38 and ~12.5 kJ/mol consistent with other calculations [17]. The shape of this potential is characteristic of all X–N–N–Y dihedrals in the other organic hydrazine derivatives. Another interesting and important feature of the hydrazines is the presence of structural isomers due to the presence of pyrimidal geometries about the nitrogen sites. This is illustrated in Fig. 3 for MMH. The left and right figures are non-superimposable due to unique geometries imparted by the lone-pair electrons. Thus, each isomer has a unique set of dihedral angles, as listed in Fig. 3, that are equal, but opposite, in sign. The FFs were developed to allow isomers to be easily simulated. The X–N–N–Y dihedrals at ~+90º and ~–90º are symmetric about the origin (Fig. 2) and easily parameterized (phase shift, δ, in eq. 1 is 0º or 180º). However, the dihedrals at approximately +150º, –150º, +30º, and –30º do not provide symmetric dihedral energy profiles. These require δ values in eq. 1 that are not 0º or 180º, hence separate FFs would be required for each isomer. Thus, in order to maximize generality, the dihedral energy parameters for each X–N–N–Y that are different than ~+90º or ~–90º were set to zero, and parameters were only assigned for the symmetric dihedrals.

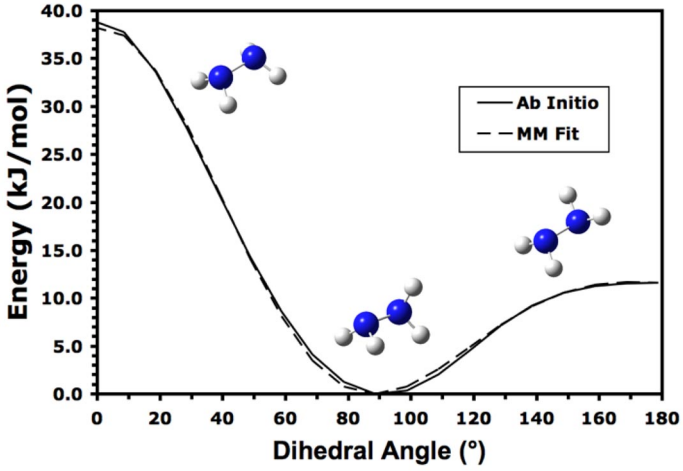

Fig. 2 HA-NH2-NH2-HB dihedral angle energy profile in N_2H_4.

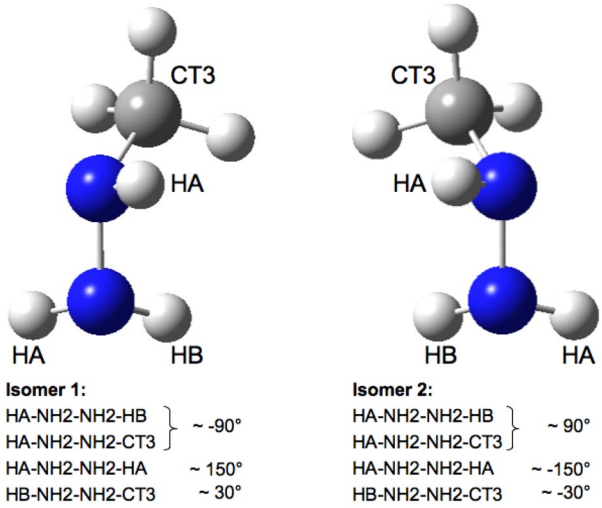

Fig. 3 Example of structural isomerism in MMH.

FFs for the monovalent hydrazinium cations $N_2H_5^+$, MMH^+, $UDMH^+$, MEH^+, and 2-HEH^+ were also developed. LJ parameters were transferred directly from the FF for the neutral hydrazines. Partial charges were reassigned based on the CHELPG procedure described above. Intramolecular parameters for bonds and angles were reassigned where necessary, i.e., for parameters involving the new atom type (NH3). The dihedrals were also reassigned, although, the complexity described in Figs. 2 and 3 is no longer present, and all dihedrals were fit directly. Parameters for NO_3^- were derived from Cadena et al. [18] and modified slightly, including reassignment of charges as described above and the introduction of improper bending parameters. All FF parameters for the hydrazinium cations and nitrate anion, including atom type assignments, are provided in the Supporting Information.

SIMULATION DETAILS

MD liquid simulations in the isothermal–isobaric (NPT) and canonical (NVT) ensembles were performed using the software NAMD [19]. Initial configurations were generated by randomly placing the appropriate number of molecules in a cubic simulation box. Equilibration of liquids was first performed to obtain converged densities, followed by NVT simulations of 3–3.5 ns at the final average densities. Pressure was controlled using a modified Nosé–Hoover method employing Langevin dynamics to control fluctuations in the barostat. Pressure was maintained (1 bar for all simulations) using barostat oscillation time and damping factors of 1 ps. Constant temperature was maintained using Langevin dynamics, with a damping factor of 5 ps^{-1}. A multiple time step algorithm was used with a 1 fs inner time step. Nonbonded interactions and full electrostatics were evaluated every 2 and 4 inner time steps, respectively. A particle mesh procedure was used for handling the electrostatics. Nonbonded interactions were truncated using a switching function with a cutoff distance of 12.0 Å and a switching onset distance of 10.0 Å. The pair list cutoff distance was set to 14.0 Å. Intramolecular LJ and Coulombic interactions between atoms separated by exactly three bonds (intramolecular 1,4-interactions) were scaled by 50 %, while interactions between fewer than three bonds were neglected. Atoms separated by three or more bonds were allowed to fully interact. For single-molecule simulations, the same procedure was followed, except computation of full electrostatics was performed.

MD simulations of the crystal structures were also performed. Initial configurations were taken directly from experimental crystallographic data. NPT simulations were performed exactly as described for the pure liquid systems with one exception. A flexible cell was used that allowed the three ortho-

gonal dimensions of the periodic cell to fluctuate independently. In the case of orthorhombic cells, all angles were held fixed at 90º. In the case of monoclinic cells, the β angle (≠90º) was allowed to vary, while the remaining angles were fixed at 90º.

The Gibbs ensemble Monte Carlo (GEMC) [20] simulation technique was used to study the vapor–liquid equilibrium (VLE) of N_2H_4, MMH, UDMH, MEH, and 2-HEH. Separate liquid- and vapor-phase boxes were constructed. Both liquid and vapor phases were given an initial temperature and density. To simulate these two coexisting phases, the NVT-GEMC method was used, which assumes a constant number of molecules ($N = N_L + N_V$), total volume ($V = V_L + V_V$) and temperature (T). In order to obtain a single VLE state point, a sequence of MC cycles were run, where a cycle is defined as N trial moves. These trial moves consisted of displacement (68 %), isotropic volume exchange (2 %), and transfer moves (30 %) which, respectively, satisfy the equality of internal equilibrium, pressures, and chemical potential between the two phases. Configurational bias [21] was used to improve the efficiency of the simulations. Simulations consisted of two stages: (i) equilibration (updates of maximum displacements occur at each cycle) and (ii) production (constant displacements). Typical runs consisted of 10 000 equilibration cycles and 20 000 production cycles. Both liquid- and vapor-phase boxes (total molecules ~260–300) were constructed using the MCCCS Towhee software [21a,22]. The number of molecules for each system were chosen to satisfy the estimated densities and to yield a box dimension that exceeds twice the size of the 12 Å cutoff.

RESULTS AND DISCUSSION

Molecular hydrazines: Force field validation

Liquid density and enthalpy of vaporization

The liquid densities of N_2H_4, MMH, and UDMH are listed in Table 7 as a function of temperature. Liquid N_2H_4 contains hydrogen-bonding between donor N–H groups and nitrogen lone-pair acceptors. Although the two lone pairs on the two nitrogens of hydrazine were not modeled explicitly, their effects were accounted for by the negative charge of –0.67 e. Extensive experimental data is available for N_2H_4 due to its prominent use as a propellant, both currently and historically [23]. The calculated liquid densities for N_2H_4 are in excellent agreement with the experimentally measured values, particularly at lower temperatures. Deviations range from +0.2 % at 298 K to –5.1 % at 450 K. Over the temperature range 273–450 K, the calculated thermal expansivity is 1.34×10^{-3} K^{-1} compared to the experimental thermal expansivity of 1.02×10^{-3} K^{-1}. Thermal expansivity was calculated from finite differences from the individual simulations carried out at different temperatures [18].

The calculated liquid densities of MMH over the temperature range of 273–450 K are lower than the experimental values [1,24]. At 273 K, the simulated density is 2.8 % lower than the experimental value, and this deviation increases to a maximum of 7.7 % at 450 K. Over the same temperature range, the calculated thermal expansivity is 1.42×10^{-3} K^{-1} compared to the experimental thermal expansivity of 1.17×10^{-3} K^{-1}. The liquid densities of MMH are lower than those of N_2H_4, attributable to the presence of the bulkier $–CH_3$ group and fewer potential hydrogen-bonding sites. In addition, both FFs perform exceptionally well at lower temperatures, but are not as reliable at higher temperatures. The simulated liquid densities for UDMH follow an opposite trend relative to MMH, with the simulated densities being greater than the experimental values [1]. Although fewer experimental densities are available, it is observed that over the temperature range of 273–339 K, the simulated values are in excellent agreement with experiment, being only slightly higher by 0.5–1.7 %. The densities of UDMH are lower than those of MMH, once again due to the presence of an additional $–CH_3$ group and fewer hydrogen-bonding sites. Over the temperature range 273–339 K, the calculated thermal expansivity is 1.12×10^{-3} K^{-1} compared to the experimental value of 1.38×10^{-3} K^{-1}.

Table 7 Liquid densities (ρ_{liq}, g/cm^3) and enthalpies of vaporization (ΔH_v, kJ/mol) of N_2H_4, MMH, and UDMH as a function of temperature (K) from MD simulations[a], compared to experimental data where available. Vapor pressures (P_{vap}, MPa) were calculated using Antoine equation fit of GEMC data.

		Temperature							
Molecule	Property	273.20	298.15	310.26	338.73	366.49	394.27	422.04	449.83
N_2H_4	ρ_{liq} (calc)	1.032 ± 0.007	1.006 ± 0.008	0.993 ± 0.008	0.961 ± 0.009	0.929 ± 0.010	0.894 ± 0.011	0.856 ± 0.013	0.814 ± 0.014
	ρ_{liq} (exp)	1.026	1.004	0.994	0.967	0.939	0.912	0.886	0.858
	ΔH_v (calc)[b]	44.10	43.18	41.80	40.58	38.91	37.03	34.85	33.05
	ΔH_v (exp)	45.94	44.77	44.22	42.93	41.71	40.46	–	–
	P_{vap} (calc)	0.0030 ± 0.0003	0.020 ± 0.001	0.015 ± 0.001	0.042 ± 0.002	0.130 ± 0.039	0.358 ± 0.032	0.845 ± 0.111	1.463 ± 0.208
MMH	ρ_{liq} (calc)	0.870 ± 0.006	0.846 ± 0.006	0.834 ± 0.007	0.807 ± 0.007	0.778 ± 0.008	0.748 ± 0.009	0.714 ± 0.010	0.676 ± 0.012
	ρ_{liq} (exp)	0.894	0.870	0.859	0.832	0.806	0.780	0.754	0.728
	ΔH_v (calc)[b]	47.78	43.51	44.64	40.58	38.16	37.36	35.31	33.01
	ΔH_v (exp)	–	40.37	–	–	36.11[c]	–	–	–
	P_{vap} (calc)	5.5e-04 ± 3e-05	0.0026 ± 0.0002	0.0052 ± 0.0003	0.021 ± 0.002	0.066 ± 0.006	0.174 ± 0.017	0.410 ± 0.045	0.867 ± 0.106
UDMH	ρ_{liq} (calc)	0.812 ± 0.005	0.791 ± 0.005	0.780 ± 0.006	0.755 ± 0.006	0.729 ± 0.006	0.702 ± 0.008	0.673 ± 0.009	0.641 ± 0.010
	ρ_{liq} (exp)	0.812	0.786	0.773	0.742	–	–	–	–
	ΔH_v (calc)[b]	45.02	43.26	43.51	40.75	38.45	37.07	34.77	32.84
	ΔH_v (exp)	–	35.23[d]	–	32.55[e]	–	–	–	–
	P_{vap} (calc)	5.44e-04 ± 2e-06	0.00230 ± 2e-05	0.00427 ± 5e-05	0.0153 ± 0.0003	0.044 ± 0.002	0.109 ± 0.006	0.238 ± 0.017	0.475 ± 0.048

[a]Calculated condensed-phase results obtained from 3.5 ns total simulation time, averaged over last 1.5 ns; calculated gas-phase properties obtained from 2 ns total simulation time, averaged over last 1.0 ns.

[b]Error bars on ΔH_v (calc) are estimated to be ~±4.18 kJ/mol based on average fluctuations in the classical gas-phase enthalpies.

[c]Enthalpy of vaporization at 364 K.

[d]NIST Webbook

[e]Enthalpy vaporization at 336 K.

Very little experimental data exists for the validation of the MEH and 2-HEH FFs. However, based on the validated FF for the smaller hydrazines, similar accuracy is expected in the liquid densities. Table 8 contains simulated liquid densities for MEH and 2-HEH. The simulated liquid densities for MEH are intermediate between MMH and UDMH. Again, addition of a CH_3–CH_2– moiety reduces the number of potential hydrogen-bonding sites, resulting in low densities relative to N_2H_4. The simulated density at 293 K is lower than the experimental value by 1.5 % [25]. The calculated thermal expansivity from 273 to 450 K is 1.22×10^{-3} K^{-1}. Interestingly, introduction of an –OH group into MEH, yielding 2-HEH, results in a significant increase in the liquid density. At 298 K, the simulated density is lower than the experimental value by 2.1 % [26]. The calculated thermal expansivity from 273 to 450 K is 6.71×10^{-4} K^{-1}, much lower than the other liquids. This large increase in density and decrease in expansivity upon introduction of a terminal –OH moiety is due to the increased potential for hydrogen bonding in the liquid. The alcoholic site can act both as a strong hydrogen donor and acceptor, giving the liquid more structure.

The FFs for the molecular hydrazines were also validated against the enthalpies of vaporization (ΔH_v) of the liquids. These results are also included in Tables 7 and 8. ΔH_v values were calculated as the difference between the gas-phase enthalpy of a single molecule and the average enthalpy per molecule in the liquid state. These were estimated from MD simulations. For these energetic quantities, a difference of ~4.2 kJ/mol or less relative to the experimental value is generally considered to be within chemical accuracy. Chemical accuracy is achieved for N_2H_4 as shown in Table 7, where the maximum difference between experiment and simulation is 3.43 kJ/mol at 394 K [27]. Experimental values are not available at higher temperatures, although the difference is observed to increase with increasing temperature. At the boiling point of H_2O, ΔH_v is 40.67 kJ/mol [28], comparable to the ΔH_v for N_2H_4 at 366 K of 41.71 kJ/mol. This is consistent with both H_2O and N_2H_4 being hydrogen-bonding liquids.

Experimental ΔH_v values for MMH and UDMH are only available at a few temperatures. At 298 and 366 K, calculated ΔH_vs for MMH are higher than the experimental values by 3.14 and 2.05 kJ/mol, respectively, both within the desired chemical accuracy [29]. At 298 and 339 K, calculated ΔH_vs for UDMH are also higher than the experimental values by 8.03 and 8.20 kJ/mol, respectively [29a,30]. These errors are considerably larger than N_2H_4 and MMH, although still in reasonable agreement with experiment. In both compounds, lower ΔH_vs relative to N_2H_4 are consistent with the presence of fewer hydrogen-bonding sites.

Calculated enthalpies of vaporization for MEH and 2-HEH are provided in Table 8. No experimental values are available for validation, although reasonable agreement is expected based on the adequate performance of the FFs for the smaller compounds. ΔH_vs for MEH are calculated to decrease from 51.04 to 37.57 kJ/mol over the temperature span from 273 to 450 K. These values are comparable in magnitude to the ΔH_vs for N_2H_4. Interestingly, introduction of the alcoholic –OH moiety in 2-HEH causes a dramatic increase in the ΔH_vs; enthalpies of vaporization range from 87.07 to 72.38 kJ/mol over the temperature span examined. This is once again attributable to the presence of hydrogen bonding due to the strong –OH donor/acceptor site. The LJ parameters for –OH were taken from the CHARMM FF for alcohols [15], with σ for oxygen being scaled down slightly (~4 %) to improve the liquid density. Although this is expected to produce reasonable results for molecular simulations, it must be noted that the strength of the hydrogen bonding in the liquid is highly dependent upon these LJ parameters. Thus, the overall FF would benefit from further experimental validation in the future.

Center-of-mass (COM) radial distribution functions (COM-COM) for the molecular hydrazines are shown in Fig. 4. In general, the hydrazines show two distinct peaks, one at short range (~3–6 Å) and another at longer range (6–12 Å). COM ordering at longer distances is not significant. The first peak in all cases is the sharpest with the greatest intensity. It is evident that these peaks shift to longer distances with increasing number of carbon atoms. The first peak for N_2H_4 occurs at 3.9 Å. MMH, with one carbon atom, has a split first peak at ~4.1 and 4.9 Å. UDMH, MEH, and 2-HEH, each with two carbon atoms, have peaks at ~5.2–5.4 Å. The second peaks indicate interactions separated by a COM and fol-

Table 8 Liquid densities (ρ_{liq}, g/cm^3) and enthalpies of vaporization (ΔH_v, kJ/mol) of MEH and 2-HEH as a function of temperature (K) from MD simulations[a], compared to experimental data where available. Vapor pressures (P_{vap}, kPa) were calculated using Antoine equation fit of GEMC data.

		Temperature								
Molecule	Property	273.20	293.20	298.15	310.26	338.73	366.49	394.27	422.04	449.83
MEH	ρ_{liq} (calc)	0.851 ± 0.005	0.833 ± 0.005	0.830 ± 0.005	0.819 ± 0.006	0.795 ± 0.006	0.769 ± 0.007	0.743 ± 0.007	0.715 ± 0.008	0.685 ± 0.010
	ρ_{liq} (exp)	–	0.846	–	–	–	–	–	–	–
	ΔH_v (calc)[b]	51.04	49.33	49.12	47.07	44.56	42.47	41.17	38.91	37.57
	ΔH_v (exp)	–	–	–	–	–	–	–	–	–
	P_{vap} (calc)	0.158 ± 0.008	0.570 ± 0.033	0.763 ± 0.045	1.496 ± 0.093	6.030 ± 0.417	19.06 ± 1.42	51.24 ± 4.19	120.94 ± 10.57	256.84 ± 23.82
2-HEH	ρ_{liq} (calc)	1.095 ± 0.004	–	1.087 ± 0.004	1.078 ± 0.005	1.060 ± 0.005	1.038 ± 0.006	1.019 ± 0.009	0.998 ± 0.007	0.976 ± 0.006
	ρ_{liq} (exp)	–	–	1.11	–	–	–	–	–	–
	ΔH_v (calc)[b]	87.07	–	86.69	85.40	84.01	80.67	77.66	76.07	72.38
	ΔH_v (exp)	–	–	–	–	–	–	–	–	–
	P_{vap} (calc)	0.112 ± 0.005	–	0.421 ± 0.020	0.741 ± 0.036	2.388 ± 0.129	6.276 ± 0.367	14.40 ± 0.90	29.63 ± 1.97	55.78 ± 3.90

[a]Calculated condensed-phase results obtained from 3.5 ns total simulation time, averaged over last 1.5 ns; calculated gas-phase properties obtained from 2 ns total simulation time, averaged over last 1.0 ns.

[b]Error bars on ΔH_v (calc) are estimated to be ~±4.18 kJ/mol based on average fluctuations in the classical gas-phase enthalpies.

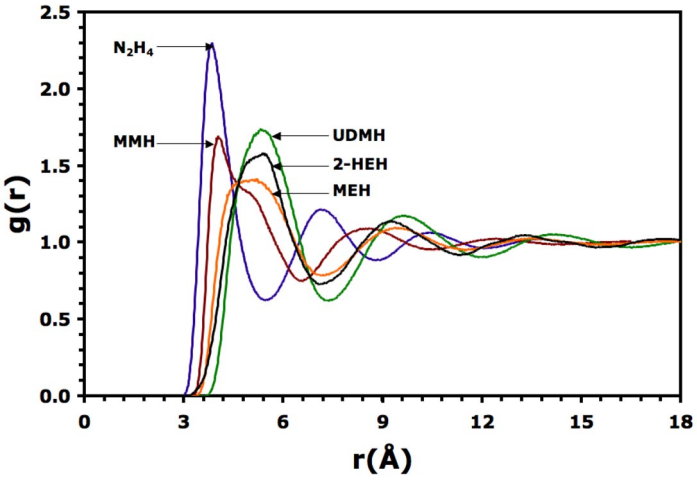

Fig. 4 COM-COM radial distribution functions for N_2H_4, MMH, UDMH, MEH, and 2-HEH.

low the same trend with increasing number of carbon atoms. The second peaks occur at ~7.2 Å for N_2H_4, followed by MMH at ~8.6 Å, and UDMH, MEH, and 2-HEH at ~9.3–9.7 Å.

Heat capacity

In general, atomistic FFs can have difficulties in accurately calculating intramolecular contributions to the overall energy or enthalpy due to approximations that are adopted in the FF itself, particularly the harmonic oscillator approximation and neglect of off-diagonal coupling terms. Thus, calculated quantities such as heat capacity, which are sensitive to intramolecular contributions, can possess relatively large errors. Simulations aimed at estimating condensed-phase heat capacities can be aided by the use of AI electronic structure calculations that can reliably predict heat capacities for isolated molecules in the gas phase. Thus, intramolecular heat capacities from ideal gas (quantum) calculations, coupled with intermolecular, or residual, contributions from simulation improve estimations of heat capacity.

The liquid heat capacity was calculated from the following expression:

$$C_P(T,P) = \left(\frac{\partial \langle H \rangle}{\partial T} \right)_P \tag{2}$$

where the enthalpy, H, is given by

$$\langle H \rangle = \left\langle H_{QM}^{IG} \right\rangle + \left\langle H_{Class}^{Res} \right\rangle \tag{3}$$

The procedure is similar to that previously described by Cadena et al. and Lagache et al. [31]. In eq. 3, H^{IG} is the ideal gas enthalpy, obtained from AI QM calculations, and H^{Res} is the residual enthalpy obtained from classical MD simulations. The vibrational contributions to the ideal gas enthalpy were scaled by 0.97. This scaling factor for calculations at the B3LYP/TZVP level was developed based on comparisons to similar small molecules [12]. The procedure of Cadena et al. was modified slightly to eliminate nonbonded intramolecular contributions from the residual heat capacity as follows:

$$\langle H \rangle = \left\langle H_{Class}^{Tot} \right\rangle - \left\langle H_{Class}^{IG} \right\rangle + \left\langle H_{QM}^{IG} \right\rangle \tag{4}$$

Here, the three terms on the right-hand side correspond to the liquid total enthalpy from classical simulations, the single-molecule ideal gas enthalpy from classical simulations, and the single-molecule ideal gas enthalpy from QM calculations, respectively. Equation 4 can further be written as follows:

$$\begin{aligned} H &= \left(U_{\text{Class}}^{\text{Tot}} + PV_{\text{Class}}^{\text{Liq}} + K\right) - \left(U_{\text{Class}}^{\text{IG}} + RT + K\right) + \left(U_{\text{QM}}^{\text{IG}} + RT + K\right) \\ H &= U_{\text{Class}}^{\text{Tot}} + PV_{\text{Class}}^{\text{Liq}} - U_{\text{Class}}^{\text{IG}} - RT + H_{\text{QM}}^{\text{IG}} \\ C_{\text{P}}^{\text{Liq}}(T,P) &= \left(\frac{\partial\langle H\rangle}{\partial T}\right)_{\text{P}} = \left(\frac{\partial\left\langle U_{\text{Class}}^{\text{Tot}}\right\rangle}{\partial T}\right)_{\text{P}} + P\left(\frac{\partial\left\langle V_{\text{Class}}^{\text{Liq}}\right\rangle}{\partial T}\right)_{\text{P}} - \frac{\partial\left\langle U_{\text{Class}}^{\text{IG}}\right\rangle}{\partial T} - R + C_{\text{P}}^{\text{IG,QM}} \end{aligned} \tag{5}$$

Thus, the overall expression for the heat capacity is given by

$$C_{\text{P}}^{\text{Liq}} = C_{\text{P}}^{\text{IG,QM}} + C_{\text{P}}^{\text{Res,Class}} = C_{\text{P}}^{\text{IG,QM}} + \left(C_{\text{P}}^{\text{Tot,Class}} - C_{\text{P}}^{\text{IG,Class}}\right) \tag{6}$$

The ideal gas contributions from classical simulations are subtracted from the total liquid contributions from classical simulations (on a per molecule basis) in order to remove intramolecular nonbonded energy contributions, which are otherwise difficult to eliminate from the total liquid energy. This assumes that the conformations sampled by the single molecule during the gas-phase MD run are similar to those sampled during the liquid simulations, although the conformational diversity is likely dampened in the liquid.

The calculated heat capacities are shown in Table 9. The ideal gas heat capacities from AI calculations for N_2H_4 and MMH are in reasonable agreement with the experimental gas-phase values, differing by 3.1 % [32] and 7.2 % [1], respectively. C_P^{IG} values calculated using the classical FFs are overestimated by as much as 60 % for the MMH case. This is indicative of the well-known fact that FFs based on simple harmonic approximations tend to overestimate the vibrational energy storage of molecules and demonstrates why direct calculation of the total heat capacity using FFs based on eq. 1 is inaccurate. On the other hand, the residual contribution to the heat capacity is significant. As shown in Table 9, the residual contribution to the heat capacity represents a large fraction of the total liquid heat capacity. For N_2H_4 and MMH, it is actually greater than $C_P^{IG,QM}$ and somewhat smaller than $C_P^{IG,QM}$ for the remaining compounds. Thus, it is critical to use the combined QM/MD approach. The calculated liquid heat capacities for N_2H_4 and MMH are in reasonable agreement with experiment to 10.3 % [27] and 9.6 % [29b], respectively, while the results for UDMH are in excellent agreement with experiment, differing by only 0.4 % [30]. Constant-pressure heat capacities for MEH and 2-HEH are predicted to be 173.38 and 191.54 J/mol·K at 298 K, although no experimental values exist for validation.

Table 9 Liquid heat capacities of molecular hydrazines (J/mol·K) at 298 K.

	Simulated[a]			Experiment	
	$C_P^{IG,QM}$	$C_P^{Res,\ Class}$	C_P^{Liq}	C_P^{Liq}	% error
N_2H_4	46.94[b]	62.05	108.99	98.82	10.3
MMH	66.02[c]	82.76	148.78	134.93	9.7
UDMH	88.20	76.40	164.60	164.01	0.4
MEH	87.28	86.10	173.38	–	–
2-HEH	102.13	89.41	191.54	–	–

[a]$C_P^{IG,QM}$ from B3LYP/TZVP level of theory, with vibrations scaled by 0.97.
[b]Exp C_P^{IG} for N_2H_4 is 48.4 J/mol·K [32].
[c]Exp C_P^{IG} for MMH is 71.1 J/mol·K [1].

Vapor–liquid equilibria

As described in the Simulation Details section, MCCCS Towhee was used to study the VLE of hydrazine and the organic derivatives. The VLE calculations were performed using the GEMC technique, where two boxes, one liquid and one vapor, are constructed and allowed to exchange molecules under NVT conditions. The simulated VLE curves for N_2H_4, MMH, UDMH, MEH, and 2-HEH are shown in Figs. 5–9, respectively. The critical density and critical temperature (both shown in Figures) were also calculated, and the results are listed in Table 10. The critical constants were obtained using an Ising model [33] as follows:

$$\rho_L - \rho_V = B \times (T_C - T)^{\beta} \tag{7}$$

$$\frac{\rho_L + \rho_V}{2} = \rho_C + A \times (T - T_C) \tag{8}$$

In eqs. 7 and 8, ρ_L and ρ_V are the liquid and vapor densities, respectively, ρ_C and T_C are the critical density and critical temperature, respectively, β is given a value of 0.32 for three-dimensional systems, and A and B are fitting constants.

Table 10 Simulated critical temperatures T_C (K) and critical densities ρ_C (g/cm^3) for N_2H_4, MMH, UDMH, MEH, and 2-HEH. Error bars were estimated as the average of the upper and lower bound to the calculated values.

	Simulation		Experiment	
	T_c	ρ_C	T_c	ρ_C
N_2H_4	593 ± 8	0.34 ± 0.01	653	0.23
MMH	595 ± 6	0.28 ± 0.01	585	0.29, 0.17
UDMH	616 ± 11	0.27 ± 0.01	523, 522	0.28
MEH	643 ± 7	0.27 ± 0.01	–	–
2-HEH	856 ± 7	0.32 ± 0.01	–	–

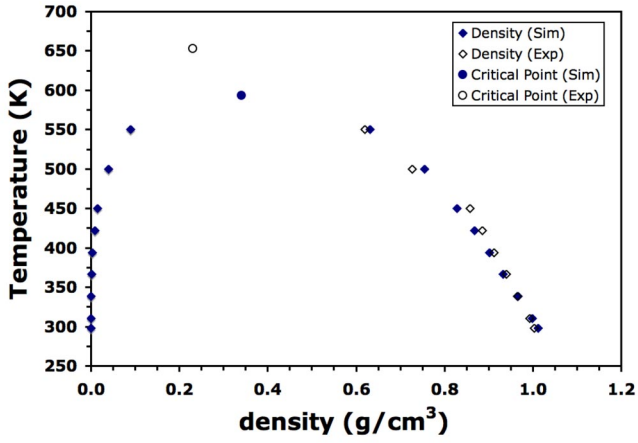

Fig. 5 VLE curve for N_2H_4.

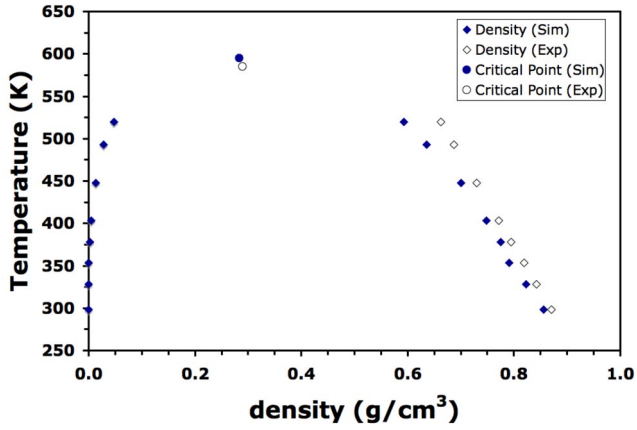

Fig. 6 VLE curve for MMH.

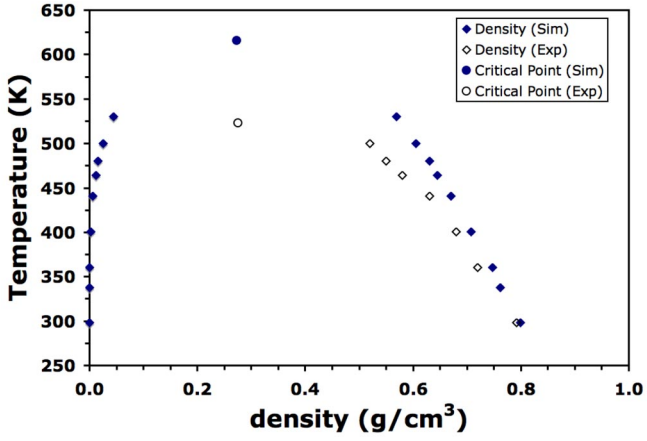

Fig. 7 VLE curve for UDMH.

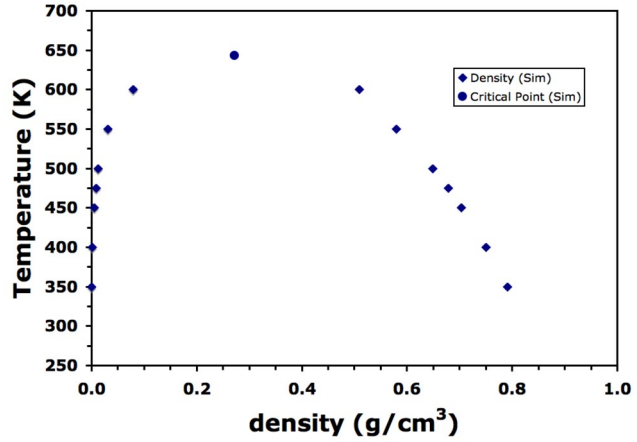

Fig. 8 Simulated VLE curve for MEH.

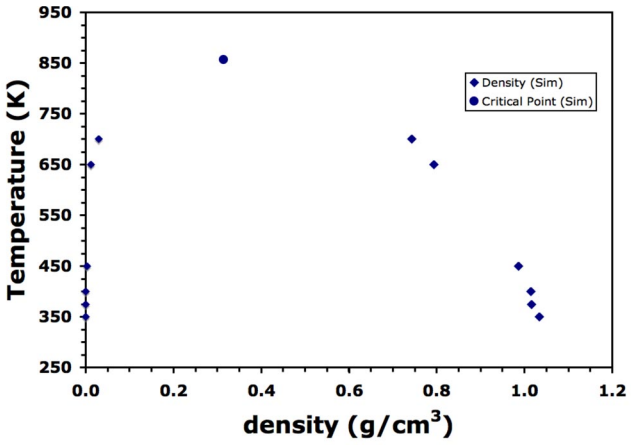

Fig. 9 Simulated VLE curve for 2-HEH.

The liquid densities from GEMC shown on the VLE curve for N_2H_4 (Fig. 5) are in excellent agreement with the experimental values as well as the MD results (Table 7). The simulated critical density and critical temperature of 0.34 g/cm^3 and 594 K are in acceptable agreement with the experimental values of 0.23 g/cm^3 and 653 K [34]. We note that it may be possible to improve the accuracy of the VLE calculations using a histogram reweighting techniques [33,35], but it is anticipated that any differences will be small.

The simulated VLE curve for MMH is in good agreement with the experimental VLE curve (Fig. 6). The GEMC liquid densities agree with the trend from the MD simulations (Table 7) compared to experiment (consistently lower). The simulated critical density and critical temperature of 0.28 g/cm^3 and 595 K are in near quantitative agreement with the experimental values of 0.29 g/cm^3 and 585 K [1,36].

Examination of Fig. 7 containing the simulated VLE curve for UDMH reveals significant differences between simulation and experiment. The GEMC liquid densities agree with those obtained from MD simulation at low temperature (Table 7). The liquid densities at high temperature from the GEMC simulation deviate strongly from the experimental values. We note, however, that the high-temperature experimental data is not very reliable, as it was estimated graphically from a published VLE curve. While the simulated critical density of 0.27 g/cm^3 is in excellent agreement with the experimental value of 0.28 g/cm^3, the simulated critical temperature is too high by almost 100 K [1,30].

While part of the difference between simulation and experimental critical points may be an indication of weakness in the FF, Schmidt [1] has noted that there is very little experimental data for hydrazine(s) near critical or supercritical conditions because the liquids undergo decomposition before the critical point is reached. Therefore, it is extremely difficult to make accurate experimental measurements of critical properties. Thus, it is not clear from the critical properties alone whether or not the FF is inaccurate.

Due to the lack of experimental VLE and critical constant data for MEH and 2-HEH, simulated results presented in Figs. 8 and 9 are pure prediction. The values of their critical constants are listed in Table 10. MEH and 2-HEH have much more conformational flexibility than N_2H_4, MMH, and UDMH, making them difficult to simulate in the NVT-GEMC ensemble at low temperatures (i.e., low acceptance percentages for MC moves). Thus, only high-temperature results were employed in the VLE analysis. The critical density and temperature for MEH were calculated to be 0.27 g/cm^3 and 643 K. This is consistent with the results for UDMH, which is reasonable as both have a similar chemical makeup, although T_C is predicted to be somewhat higher than that of UDMH. As mentioned previously, hydrogen bonding is substantial in 2-HEH, and therefore the liquid properties are sensitive to the LJ

parameters and charges. Although critical constants have been predicted, validation would provide more reassurance of the reliability of the FF for this somewhat complicated molecule. The presence of the –OH moiety has a dramatic effect on the critical constants. High-temperature simulations were necessary to sample enough phase space to make reasonable predictions. The critical density and temperature were calculated to be 0.32 g/cm^3 and 856 K for 2-HEH. These are significantly different from those previously calculated for the simpler hydrazines.

Dynamics

It is well established that the self-diffusion coefficient for a fluid can be calculated using the Einstein relation [37]

$$D_s = \frac{1}{6}\lim_{t\to\infty}\frac{d}{dt}\left\langle \left|\vec{r}(t)-\vec{r}(0)\right|^2 \right\rangle \tag{9}$$

where the bracketed quantity represents the mean squared displacement (MSD). It is critical that the system exhibit true diffusive motion, which can be identified by $\gamma \approx 1$ calculated from the following expression:

$$\gamma(t) = \frac{d(\log(\Delta r^2))}{d(\log(t))} \tag{10}$$

where Δr^2 is the COM MSD over time t. Subdiffusive behavior is characterized by $\gamma < 1$. All the species except 2-HEH had $\gamma \approx 1$. Therefore, self-diffusion coefficients were estimated for N_2H_4, MMH, UDMH, and MEH, and are listed in Table 11 at 298 K, along with standard deviations. The D_s value for N_2H_4 is 7.6×10^{-10} m^2/s. As a comparison, the self-diffusion coefficient of H_2O is 2.2×10^{-9} m^2/s [38], which is roughly 3 times higher than N_2H_4. This result is reasonable considering that the mass of N_2H_4 is ~2 times greater than that of H_2O. Replacing a hydrogen on N_2H_4 with a methyl group to yield MMH slows down the translational dynamics by about one-half, consistent with the expected behavior for a larger molecule. Upon addition of a second methyl group to form UDMH, the dynamics speed up again. This could possibly be attributed to the reduction in the number of hydrogen-bonding sites (electropositive HA or HB). In the case of MEH, where once again there are three free hydrogens (HA or HB) available for hydrogen bonding, the translational dynamics slow down slightly relative to UDMH. Finally, the self-diffusion coefficient of 2-HEH could not be computed on the time scale of the simulations due to $\gamma < 1$. We can say, however, that the translational dynamics are much slower than the other four hydrazines. It is well known that the introduction of an –OH moiety can dramatically dampen the dynamics [39] due to persistent hydrogen bonds.

Table 11 Self-diffusion coefficients (D_s, $\times 10^{10}$ m^2/s) and rotational time constants (τ, ps) for molecular hydrazines at 298 K.

	D_s	τ_{Rot}
N_2H_4	7.6 ± 0.2	2.3
MMH	3.6 ± 0.3	11.2
UDMH	4.8 ± 0.1	4.9
MEH	2.8 ± 0.1	20.9
2-HEH	–[a]	25.6×10^3

[a]Subdiffusive on time scale of simulation (3 ns).

As an additional metric of system dynamics, the rotational time constant was calculated for each species using the following correlation function:

$$C(t) = \left\langle \frac{1}{2}[3\cos^2 \theta_i(t) - 1] \right\rangle \tag{11}$$

where $\theta_i(t)$ is the angle of a vector formed between itself at time t and the original vector at time $t = 0$. $C(t)$ will decay to zero as the molecule loses its orientational correlation [40]. The rotational correlation time constant, τ, was computed for each species by assigning the vector in eq. 11 to the longest principal axis of the species and using the following relation:

$$\tau = \int_0^\infty C(t)\, dt \tag{12}$$

where $C(t)$ was fit to a stretched exponential of the form

$$C(t) = a_0 e^{-\left(\frac{t}{\tau_0}\right)^\beta} \tag{13}$$

where a_0 is a constant, τ_0 is the rotational time constant at $t = 0$, and β is a stretching parameter. The rotational time constants at 298 K for the hydrazines are also listed in Table 11. These results parallel the self-diffusion results. The 2.3 ps rotational time constant for N_2H_4 is consistent with the ~2 ps constant for water [41], a hydrogen-bonding fluid. The rotational dynamics of MMH decrease relative to N_2H_4, while the rotational dynamics of UDMH are faster than those of MMH. This is consistent with fewer amine hydrogens and with the self-diffusion coefficient results. The rotational time constant for MEH is larger than that of MMH as expected. Once again, the introduction of the –OH moiety causes a staggering decrease in the rotational dynamics of 2-HEH. The simulations predict that the rotational time constant for 2-HEH is about 26 ns, significantly longer than the other species.

It is instructive to compare the experimental viscosities of these hydrazines to the results obtained for the translational and rotational dynamics. The estimated dynamic/absolute experimental viscosities at 298 K for N_2H_4, MMH, UDMH, and 2-HEH are 0.913 cP [23a], 0.775 cP [1], 0.492 cP [1], and 147 cP [1]. Although a perfect correlation is not possible, it is interesting to note that UDMH has a lower viscosity than MMH, consistent with the simulation results above. Also, the experimental viscosity of 2-HEH is 300 times greater than that of UDMH. Thus, experimental results confirm the dampening of system dynamics with the addition of –OH. Future simulations of viscosity (e.g., with RNEMD [42]) could possibly aid in refining the FF.

ENERGETIC HYDRAZINIUM SALTS AND IONIC LIQUIDS

The intermolecular LJ FF parameters developed and validated for the molecular hydrazines were transferred directly to a hydrazinium (+1) FF. Charges were recalculated for each cation; intramolecular bond, angle, and dihedral parameters containing the new atom type (NH3) were reassigned. These FF parameters are listed in the Supporting Information (including the NO_3^- FF). As an initial test of the performance of the hydrazinium FF, the experimental crystal structures of hydrazinium nitrate ($[N_2H_5][NO_3]$) [43], methylhydrazinium nitrate ($[MMH][NO_3]$) [44], and 1,1-dimethylhydrazinium nitrate ($[UDMH][NO_3]$) [44] were simulated using MD.

The resultant simulated crystal structures are shown in Fig. 10 for $[N_2H_5][NO_3]$, $[MMH][NO_3]$, and $[UDMH][NO_3]$. Side-by-side figure comparisons are to scale. A comparison of the calculated and experimental lattice parameters and lattice density is given in Table 12. The simulated monoclinic $[N_2H_5][NO_3]$ shows moderate distortion compared to the X-ray lattice structure. Although the zig-zag pattern along the **a**-axis direction is maintained, there are considerable thermal fluctuations. The lattice

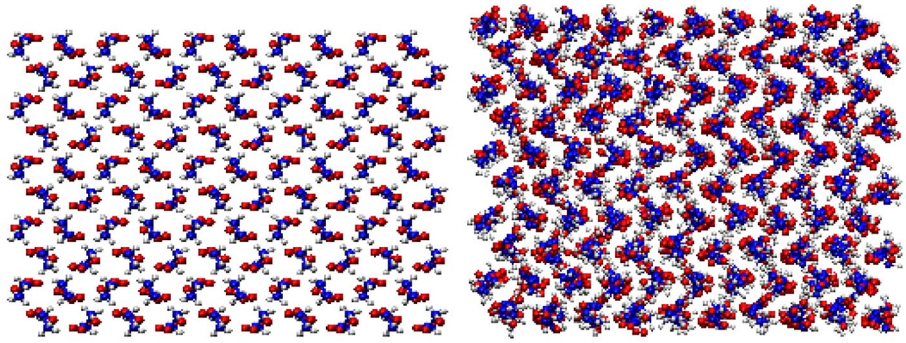

$[N_2H_5][NO_3]$

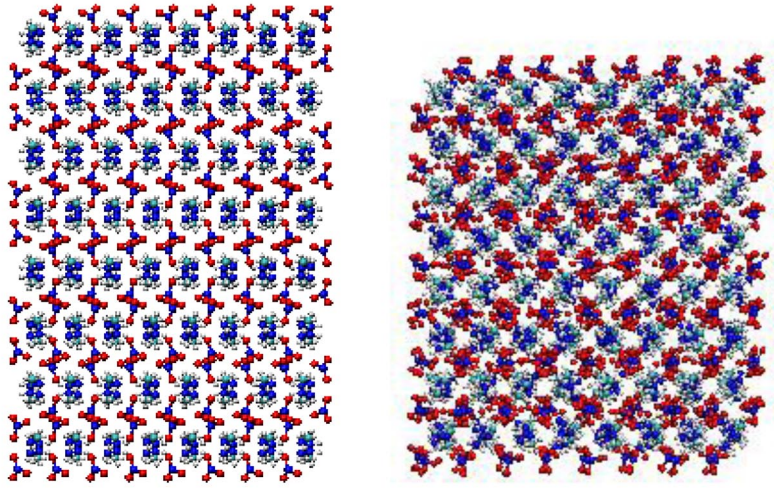

$[MMH][NO_3]$

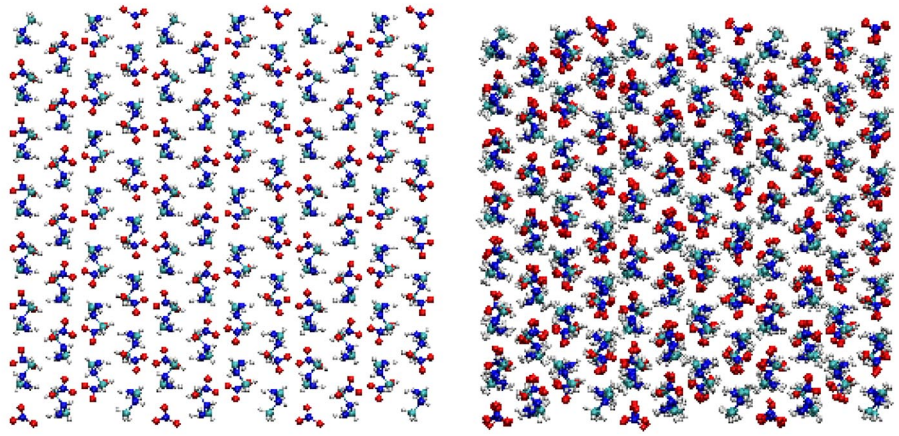

$[UDMH][NO_3]$

Fig. 10 Experimental (left) and simulated (right) crystal structures of $[N_2H_5][NO_3]$ (top, 120 K), $[MMH][NO_3]$ (middle, 200 K), and $[UDMH][NO_3]$ (bottom, 200 K). Direction → represents **a** axis and direction ↑ represents **b** axis. Axis **c** is perpendicular to page.

contracts in the **a** and **c** directions by 5.5 and 2.9 %, respectively, and expands in the **b** direction by 3.5 %. The β angle is in very good agreement with the experimental angle, differing by only 0.04 %. Overall, a reasonable agreement is observed with experiment despite the distortion in the cell. The simulated density is only 5.2 % greater than the experimental value.

Table 12 Simulated solid (crystal) and liquid (above experimental melting points at 348 K) properties of $[N_2H_5][NO_3]$, [MMH][NO_3], and [UDMH][NO_3]. Note that self-diffusivities (D_s) are approximate due to the fact that $\gamma < 1$ for these systems.

	$[N_2H_5][NO_3]$[a]			[MMH][NO_3][b]			[UDMH][NO_3][c]		
	Sim	Exp	% error	Sim	Exp	% error	Sim	Exp	% error
Crystal									
a (Å)	7.527	7.965	–5.5	4.377	3.779	+15.8	14.219	14.039	+1.3
b (Å)	5.863	5.657	+3.5	10.083	11.342	–11.1	5.729	5.649	+1.4
c (Å)	7.883	8.122	–2.9	11.331	11.107	+2.0	7.332	7.603	–3.6
β (°)	91.30	91.34	–0.04	100.33	99.09	+1.3	90.0	90.0	–
ρ (g/cm^3)	1.816	1.726	+5.2	1.473	1.542	–4.5	1.370	1.357	+1.0
Liquid[d]									
ρ (g/cm^3)	1.681	–	–	1.376	–	–	1.230	–	–
V_M (cm^3/mol)	56.6	–	–	79.3	–	–	100.1	–	–
D_s^+ ($\times 10^{12}$ m^2/s)	2.25 ± 0.22	–	–	5.58 ± 0.37	–	–	4.49 ± 0.22	–	–
D_s^- ($\times 10^{12}$ m^2/s)	2.90 ± 0.23	–	–	7.92 ± 0.37	–	–	6.50 ± 0.44	–	–
τ_{Rot}^+ (ps)[e]	289.3	–	–	264.9	–	–	297.2	–	–
τ_{Rot}^- (ps)[e]	869.0	–	–	217.6	–	–	199.8	–	–

[a]500 pairs, 120 K crystal.
[b]512 pairs, 200 K crystal.
[c]420 pairs, 200 K crystal.
[d]Simulated at 348 K.
[e]Longest molecular axis.

The simulated lattice for [MMH][NO_3] shows major distortions compared to the experimental X-ray structure. Thus, the FF is unsuccessful in simulating the experimental monoclinic crystal phase. The regular repeating pattern of the experimental structure is no longer visible, and thermal fluctuations are dramatic. As seen in the figure, the simulated crystal expands in the **a** direction by 15.8 % and contracts in the **b** direction by 11.1 %. Distortion in the perpendicular **c** direction is minor at 2.0 %. Moreover, the β angle increases by over 1° (1.3 %). The nearly equal and opposite distortions in **a** and **b** axes allow the simulated density to remain in good agreement with the experimental density, being only 4.5 % lower, an entirely fortuitous result. In the experimental structure, considerable free volume is observed, and upon closer inspection, the nitrate anions are stacked in eclipsed columns. However, upon simulation, the nitrates remain stacked, but in an irregular fashion, accompanied by a decrease in the free volume of the cell.

The simulated lattice for [UDMH][NO_3] is in excellent agreement with the experimental orthorhombic X-ray structure. Aside from small thermal fluctuations, the simulated lattice retains its shape and symmetry relative to the crystal lattice. Deviations in the **a**, **b**, and **c** axes are +1.3, +1.4, and –3.6 %, respectively. The cell angles were not allowed to vary from their 90° ideal values. The simulated density is only 1.0 % lower than the experimental density.

Interestingly, the nitrate anions in the experimental lattices of $[N_2H_5][NO_3]$ and [UDMH][NO_3] are not stacked in an apparent regular fashion as in [MMH][NO_3], but rather appear staggered. The simulated lattices of the former two crystals, coincidentally or not, show the smallest deviations from experiment. However, some may argue that the deviations in $[N_2H_5][NO_3]$ are important. Nonetheless, a

possible reason for large errors in the [MMH][NO_3] simulated phase may be due to limitations in the nitrate FF, and the driving force to maximize hydrogen-bonding interactions via irregularities in the stacking of the anion. Otherwise, the poor performance of the methylhydrazinium FF, in light of the exceptional performance for neutral MMH, is inexplicable.

[N_2H_5][NO_3], [MMH][NO_3], and [UDMH][NO_3] have melting points below 100 °C, and thus may be considered as ILs. The liquids were simulated at 348 K, above the melting points of all three salts. The liquid properties are listed in Table 12. All three have very high densities at the simulated temperature, decreasing from 1.681 g/cm^3 for [N_2H_5][NO_3] to 1.230 g/cm^3 for [UDMH][NO_3]. As the density decreases, the molar volume increases across the hydrazinium series. The molar volume of [UDMH][NO_3] is nearly twice that of [N_2H_5][NO_3]. The self-diffusion coefficients (eq. 9) and rotational time constants (eq. 12) were also evaluated for the cation and anion of each salt. The simulations predict that the salts have much slower translational dynamics than the corresponding molecular liquids. In each salt, the anion exhibits faster translations dynamics than the cation (larger D_s values). Additionally, [N_2H_5][NO_3] exhibits faster dynamics overall relative to [MMH][NO_3] and [UDMH][NO_3]. All are on the order of 10^{-12} m^2/s, although $\gamma < 1$ (eq. 10), suggesting that the 3 ns simulations are inadequate to sample the diffusive regime. Rotational time constants for the cations and anions of each IL are on the order of several hundred picoseconds.

The hydrazinium salt, 2-hydroxyethylhydrazinium nitrate (2-HEHN), as mentioned in the Introduction, is a low-melting IL that has considerable potential to replace current hazardous materials in energetic applications, such as those involving propellants. Although little experimental data is available in the literature, the physical and dynamical properties of this IL are predicted based on previous validation of the molecular FF for the neutral hydrazines. As shown in Fig. 11, the liquid densities decrease linearly with increasing temperature. The experimental density at 298 K of 1.42 g/cm^3 is in excellent agreement with the simulated value of 1.428 g/cm^3 [45]. The liquid structure was evaluated via radial distribution analysis of the system components. The cation–cation, cation–anion, and anion–anion COM-COM radial distribution functions are shown in Fig. 12. The attractive cation–anion (+–) g(r) is the most intense and occurs at the shortest distance of 4 Å. A significant cation–anion longer-range interaction occurs at ~9 Å. The repulsive cation–cation (++) and anion–anion (– –) interactions are less intense and occur at longer distances of 5.7 and 7.3 Å, respectively. It is observed that there are three distinct anion–anion peaks at short distances less than 8 Å. This is indicative of the fact that there are three sites on the cation with which the anion can interact; two nitrogen sites and the hy-

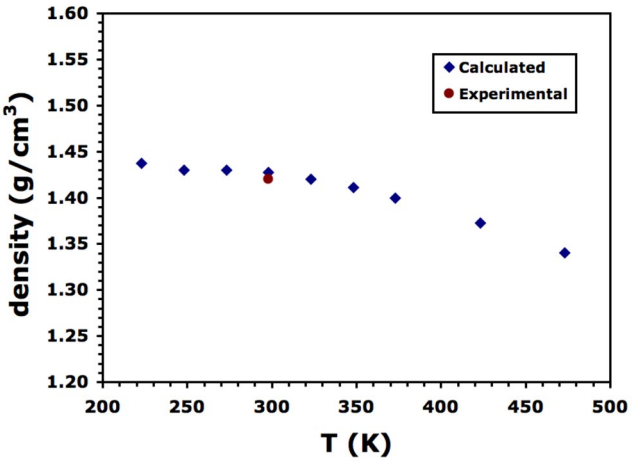

Fig. 11 Simulated liquid density (g/cm^3) of 2-HEHN vs. temperature (K). Experimental data point is from ref. [45].

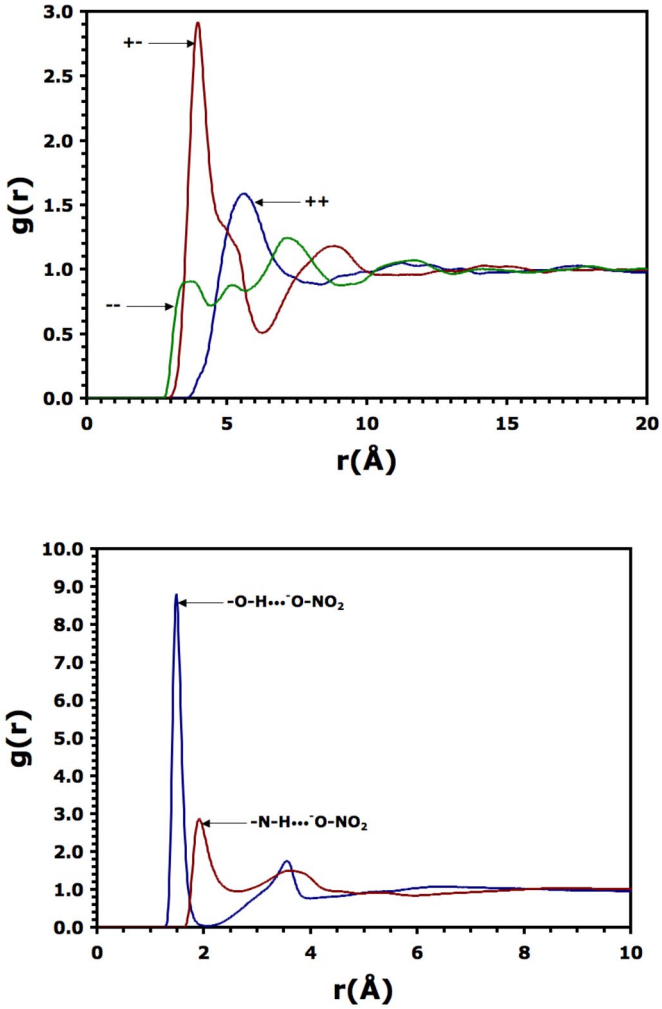

Fig. 12 (Top) COM-COM radial distribution functions for cation/cation (++), cation/anion (+–), and anion/anion (––) interactions in 2-HEHN at 298 K. (Bottom) Site-site radial distribution functions for hydroxyl:nitrate interactions and amine:nitrate interactions in 2-HEHN at 298 K.

droxyl site. The anion–anion peaks are weak secondary peaks induced by the three primary cation–anion interactions. The cation–cation and anion–anion also show weaker correlations at about 12 Å.

As described previously for 2-HEH, the IL 2-HEHN is expected to exhibit strong hydrogen bonding in the liquid. As shown in Fig. 12, the major hydrogen-bonding interactions between the cation and anion have been evaluated using a pair distribution function analysis. Here, the interaction between the nitrate oxygen atoms and either the hydroxyl hydrogen or amine hydrogens of 2-HEH$^+$ has been studied. The N–H···O interaction is far weaker than the O–H···O interaction. The former occurs at ~1.9 Å while the latter occurs at the much shorter distance of ~1.5 Å. The hydrogen bond of 1.5 Å is very short relative to hydrogen bonds in general [46], and suggests that this interaction is very strong in the liquid. This is supported by the sharpness and intensity of the g(r) curve for this peak relative to the N–H···O interaction. These hydrogen-bonding correlations at 1.5 and 1.9 Å are entirely consistent with the COM-COM anion–anion correlations noted above. The correlations at about 3.5–4 Å are associated with the neighboring oxygens of the nitrate anion. The information provided by these g(r) curves is ev-

idence of an IL that is dominated by hydrogen bonding due to the presence of many significant donor/acceptor sites.

The dynamics of 2-HEHN were probed by calculating the MSD vs. time for the cation and anion, as well as their self-diffusion coefficients (eq. 9). The temperature dependence of the dynamics was evaluated over the temperature range of 223–473 K. Figure 13 shows the MSD (Å^2) vs. temperature (K) at four different observation times. As noted by Jiang et al. [39], information about the melting/glass-transition region for an IL can be elucidated from the MSD vs. temperature curve in the region where the ions exhibit small fluctuations (<0.1 Å^2), indicating lack of global motion. In Fig. 13, the MSDs increase rapidly at higher temperature, making it difficult to distinguish behavioral characteristics at lower temperatures in the plot. Thus, the breakout plots illustrate behavior over the entire temperature range

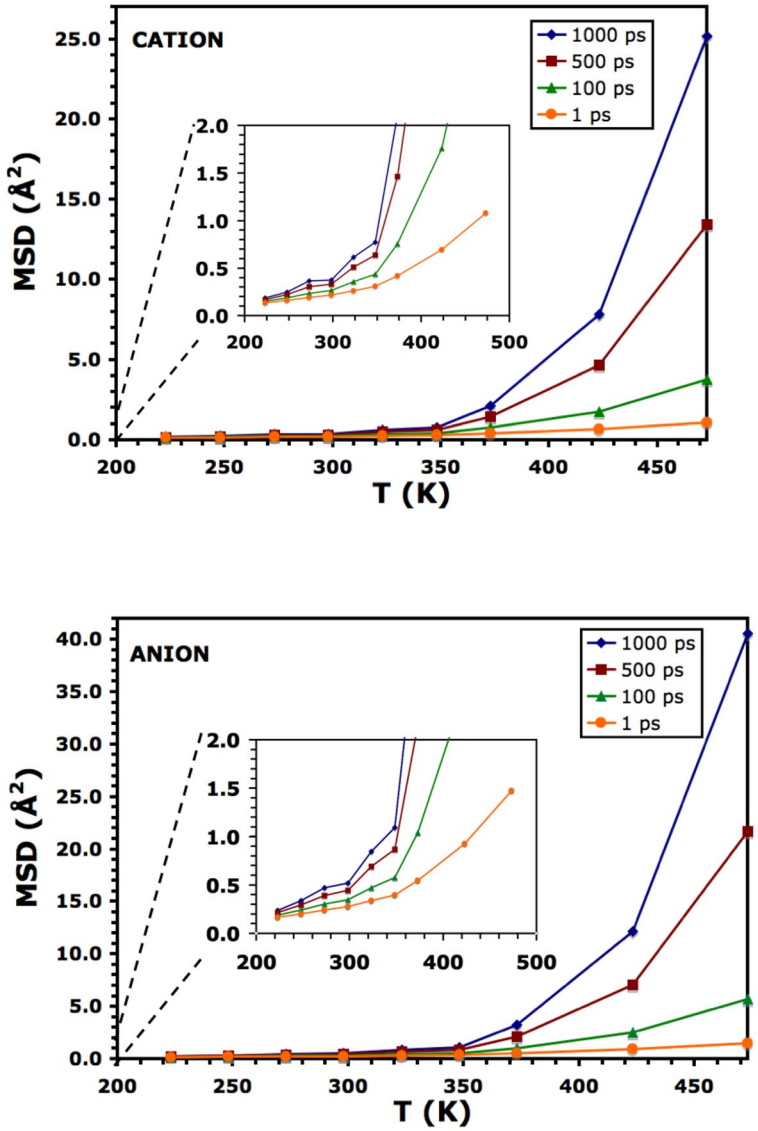

Fig. 13 Simulated temperature dependence of 2-HEHN cation (top) and anion (bottom) MSDs (Å^2) at several elapsed times.

focusing on smaller MSDs. As seen in the two figures for the cation and anion at temperatures below about 250 K, motion over the 1000 ps observation range is <0.1 $Å^2$, indicating glassy behavior. However, above 250 K, displacements over the 1000 ps timeframe are greater than 0.1 Å and mark the start of rapidly accelerating displacements with temperature increase. Qualitatively, this is in good agreement with the reported melting point of 2-HEHN of <248 K [45]. Further studies of melting point using pseudo-supercritical path sampling methods [47] will allow quantitative confirmation of the melting point given by this model.

Self-diffusion coefficients were estimated from the MSD vs. time relations using eq. 9. The γ values from eq. 10 over the 3 ns simulations indicate that at the lower temperatures, the cation and anion of 2-HEHN exhibit subdiffusive behavior, making it impossible to quantitatively assign D_s. Thus, the values in Table 13 are "apparent" self-diffusion coefficients, and much longer simulations are required. As shown in Table 13, at low temperatures in the range of 223–348 K, the translational motion of the ions is very small, with apparent self-diffusivities on the order of 10^{-13} m^2/s, much smaller than those previously reported for ILs [18,31a]. This slow behavior is likely attributable to the strong hydrogen-bonding behavior of the IL. At temperatures of 373 K and above, a speed-up in the dynamics is observed. At the highest temperature of 473 K, the self-diffusivities are ~4×10^{-11} and ~6×10^{-11} m^2/s for the cation and anion, respectively. The hydrogen bonds are labile in this temperature region, allowing the species to move more freely in the bulk. We note, however, that employing dampened charges or using a polarizable FF may yield more accurate dynamics for these systems [48].

Table 13 Calculated apparent self-diffusion coefficients (D_s, × 10^{13} m^2/s) of 2-HEHN cation and anion.

T(K)	D_s^+	D_s^-
223	0.5 ± 0.2	0.6 ± 0.3
248	0.8 ± 0.3	1.3 ± 0.4
273	1.4 ± 0.4	2.0 ± 0.4
298	1.2 ± 0.4	1.9 ± 0.6
323	3.0 ± 0.7	4.4 ± 0.9
348	3.5 ± 0.8	5.9 ± 0.9
373	18.7 ± 2.2	33.6 ± 4.6
423	109 ± 8	166 ± 8
473	383 ± 29	609 ± 21

CONCLUSIONS

An internally consistent, atomistic FF for the simulation of molecular hydrazines, including N_2H_4, MMH, UDMH, MEH, and 2-HEH, has been developed using a combination of AI and MM calculations. For the neutral compounds, the FF was validated against several thermochemical properties, including liquid density, enthalpy of vaporization, heat capacity, vapor–liquid coexistence curves, and vapor pressures. Overall, the FFs yielded results that were in reasonable agreement with available experimental data. Liquid densities were predicted to within a few percent, and near chemical accuracy (<8.4 kJ/mol) in the enthalpies of vaporization were achieved. Liquid heat capacities were also reliably predicted using a combined approach that coupled gas-phase heat capacities from AI calculations with residual heat capacities from MD simulations. The maximum error in heat capacity was ~10 % for N_2H_4. The VLE curves for the five hydrazines were also predicted using GEMC simulations. The VLE curves for N_2H_4 and MMH were in excellent agreement with the experimental curves, while larger deviations were observed for UDMH, particularly at higher temperature. The critical temperature and density for MMH and N_2H_4 were in near quantitative agreement with the experimental values. The critical

temperature of UDMH was overestimated by about 100 K. Considering the significant uncertainty in the quality of the experimental values due to difficulty in making measurements, the simulated VLE properties are acceptable. The simulations predict that the dynamics of HEH are much slower than for the other four compounds, in agreement with experimental viscosity trends.

Having validated the FF for the molecular hydrazines, LJ parameters were transferred directly into a hydrazinium (+1) FF. Charges were recalculated according to previous procedure, and intramolecular parameters were reassigned where needed. The FF was rigorously tested on a series of 1:1 hydrazinium nitrate salts, including $[N_2H_5][NO_3]$, [MMH][NO_3], and [UDMH][NO_3]. Using the experimental crystal structures, the solids were simulated at low temperatures, and the liquids were simulated above their melting points. The simulated crystal structure [UDMH][NO_3] was in excellent agreement with experiment, while that for $[N_2H_5][NO_3]$ was in reasonable agreement. The simulated structure of [MMH][NO_3] was poorly reproduced and was attributed to difficulties in simulating the stacking of nitrate anions. Liquid-phase densities, self-diffusion coefficients, and rotational time constants were predicted for these compounds; there are no experimental data to compare with.

Predictions of the static and dynamics properties of 2-HEHN were made. The simulated liquid density was within 1 % of the reported experimental value. In addition, the temperature dependence of the MSD of the cation and anion at several observation times indicated the lack of global ion motion below ~250 K. This is qualitatively consistent with the experimentally reported melting point of <248 K, although further studies using established simulation protocols could aid in a quantitative assessment of the melting point. Difficulty was encountered in assigning quantitative self-diffusion coefficients for the cation and anion of 2-HEHN due to subdiffusive behavior on the simulation time scale.

The FF developed herein for molecular hydrazines and hydrazinium salts marks an initial effort to aid experimentalists and theorists in the study of this interesting class of materials. The FF is readily extendable to more complex types of hydrazines or related compounds using the development procedure described herein. The lack of experimental data, however, makes it crucial that development procedures and simulation protocols are reliable and transferrable. Nonetheless, the energetic qualities associated with hydrazines and related compounds make their simulation a desirable component of any research or development effort. The ability to reliably simulate hydrazinium compounds will make this possible.

SUPPORTING INFORMATION

The Supporting Information contains all FF parameters for the hydrazinium (+1) cations and the nitrate anion and is available online (doi:10.1351/PAC-CON-08-09-24).

ACKNOWLEDGMENTS

Funding was provided by the Air Force Office of Scientific Research under Grant No. FA9550-07-1-0443.

REFERENCES

1. E. W. Schmidt. *Hydrazine and Its Derivatives: Preparation, Properties, and Applications*, 2nd ed. (2 volumes), John Wiley, New York (2001).
2. L. G. Cole, E. C. Gilbert. *J. Am. Chem. Soc.* **73**, 5423 (1951).
3. U.S. Environmental Protection Agency. *Integrated Risk Information System (IRIS) on Hydrazine/Hydrazine Sulfate*, National Center for Environmental Assessment, Office of Research and Development, Washington, DC (1999).

4. Health Council of the Netherlands. N-*Methylhydrazine: Evaluation of the Carcinogenicity and Genotoxicity*, The Hague, Health Council of the Netherlands (2002). Publication no. 2002/07OSH.
5. International Agency for Research on Cancer (IARC). *IARC Monographs on the Evaluation of the Carcinogenic Risk of Chemicals to Man: Some Aromatic Amines, Hydrazine and Related Substances, N-Nitroso Compounds and Miscellaneous Alkylating Agents*, Vol. 4, World Health Organization, Lyon (1974).
6. "US missile destroys toxic tank on spy satellite", *Nature* **451**, 1041 (2008).
7. (a) V. Bombelli, M. Ford, T. Marée. *Proc. 2nd Int. Conf. on Green Propellants for Space Propulsion*, Calgari, Sardinia, Italy (7–8 June 2004). ESA SP-557, October 2004; (b) E. W. Schmidt, E. J. Wucherer. *Proc. 2nd Int. Conf. on Green Propellants for Space Propulsion*, Calgari, Sardinia, Italy (7–8 June 2004), ESA SP-557, October 2004.
8. A. J. Brand, G. W. Drake. "Energetic hydrazinium salts", U.S. Patent 6218577, filed 16 July 1999, issued 17 April 2001.
9. (a) E. M. Cabaleiro-Lago, M. A. Rios. *J. Phys. Chem. A* **103**, 6468 (1999); (b) V. Dyczmons. *J. Phys. Chem. A* **104**, 8263 (2000); (c) X.-H. Ju, H.-M. Xiao. *J. Mol. Struct. (Theochem)* **588**, 79 (2002).
10. Gaussian 03, Revision D.01, M. J. Frisch, G. W. Trucks, H. B. Schlegel, G. E. Scuseria, M. A. Robb, J. R. Cheeseman, J. A. Montgomery, Jr., T. Vreven, K. N. Kudin, J. C. Burant, J. M. Millam, S. S. Iyengar, J. Tomasi, V. Barone, B. Mennucci, M. Cossi, G. Scalmani, N. Rega, G. A. Petersson, H. Nakatsuji, M. Hada, M. Ehara, K. Toyota, R. Fukuda, J. Hasegawa, M. Ishida, T. Nakajima, Y. Honda, O. Kitao, H. Nakai, M. Klene, X. Li, J. E. Knox, H. P. Hratchian, J. B. Cross, V. Bakken, C. Adamo, J. Jaramillo, R. Gomperts, R. E. Stratmann, O. Yazyev, A. J. Austin, R. Cammi, C. Pomelli, J. W. Ochterski, P. Y. Ayala, K. Morokuma, G. A. Voth, P. Salvador, J. J. Dannenberg, V. G. Zakrzewski, S. Dapprich, A. D. Daniels, M. C. Strain, O. Farkas, D. K. Malick, A. D. Rabuck, K. Raghavachari, J. B. Foresman, J. V. Ortiz, Q. Cui, A. G. Baboul, S. Clifford, J. Cioslowski, B. B. Stefanov, G. Liu, A. Liashenko, P. Piskorz, I. Komaromi, R. L. Martin, D. J. Fox, T. Keith, M. A. Al-Laham, C. Y. Peng, A. Nanayakkara, M. Challacombe, P. M. W. Gill, B. Johnson, W. Chen, M. W. Wong, C. Gonzalez, J. A. Pople, Gaussian, Inc., Wallingford CT (2004).
11. (a) A. D. Becke. *J. Chem. Phys.* **98**, 5648 (1993); (b) A. D. Becke. *J. Chem. Phys.* **98**, 1372 (1993); (c) C. Lee, W. Yang, R. G. Parr. *Phys. Rev. B* **37**, 785 (1988); (d) N. Godbout, D. R. Salahub, J. Andzelm, E. Wimmer. *Can. J. Chem.* **70**, 560 (1992).
12. NIST Computational Chemistry Comparison and Benchmark Database, R. D. Johnson III (Ed.), NIST Standard Reference Database Number 101 (Release 14 Sept 2006). <http://srdata.nist.gov/cccbdb>.
13. C. M. Breneman, K. B. Wiberg. *J. Comp. Chem.* **11**, 361 (1990).
14. W. Damm, A. Frontera, J. Tirado-Rives, W. L. Jorgensen. *J. Comp. Chem.* **18**, 1955 (1998).
15. (a) A. D. MacKerell Jr., J. Wiorkiewicz-Kuczera, M. Karplus. *J. Am. Chem. Soc.* **117**, 11946 (1995); (b) N. Foloppe, A. D. MacKerell Jr. *J. Comp. Chem.* **21**, 86 (2000); (c) A. D. MacKerell Jr., N. Banavali. *J. Comp. Chem*. **21**, 105 (2000).
16. J. N. Canongia Lopes, J. Deschamps, A. A. H. Padua. *J. Phys. Chem. B* **108**, 2038 (2004).
17. L. Radom, W. J. Hehre, J. A. Pople. *J. Am. Chem. Soc*. **94**, 2371 (1972).
18. C. Cadena, E. J. Maginn. *J. Phys. Chem. B* **110**, 18026 (2006).
19. L. Kale, R. Skeel, M. Bhandarkar, R. Brunner, A. Gursoy, N. Krawetz, J. Philips, A. Shinozaki, K. Varadarajan, K. Schulten. *J. Comp. Chem*. **151**, 283 (1999).
20. A. Z. Panagiotopoulos. *Mol. Simul*. **9**, 1 (1992).
21. (a) M. G. Martin, J. I. Siepmann. *J. Phys. Chem. B* **103**, 4508 (1999); (b) J. I. Siepmann, D. Frenkel. *Mol. Phys.* **75**, 59 (1992).
22. M. G. Martin, available from: <http://towhee.sourceforge.net>.

23. (a) R. C. Ahlert, G. L. Bauerle, J. V. Lecce. *J. Chem. Eng. Data* **7**, 158 (1962); (b) L. D. Barrick, G. W. Drake, H. L. Lochte. *J. Am. Chem. Soc.* **58**, 160 (1936); (c) P. Walden, H. Hilgert. *Z. Phys. Chem*. **165A**, 241 (1933).
24. R. C. Ahlert, C. J. Shimalla. *J. Chem. Eng. Data* **13**, 108 (1968).
25. A. N. Kost, R. Sagitullin. *J. Gen. Chem. USSR* **33**, 855 (1963).
26. In *The Merck Index*, S. Budavi (Ed.), p. 817, Merck, Whitehouse Station, NJ (1996).
27. D. W. Scott, G. D. Oliver, M. E. Gross, W. N. Hubbard, H. M. Huffman. *J. Am. Chem. Soc.* **71**, 2293 (1949).
28. In *CRC Handbook of Chemistry and Physics*, 88th ed., D. R. Lide (Ed.), Taylor and Francis, Boca Raton (2008).
29. (a) V. Majer, V. Svoboda. *Enthalpies of Vaporization of Organic Compounds: A Critical Review and Data Compilation*, p. 300, Blackwell Scientific, Oxford (1985); (b) J. G. Aston, H. L. Finke, G. J. Janz, K. E. Russell. *J. Am. Chem. Soc*. **73**, 1939 (1951).
30. J. G. Aston, J. L. Wood, T. P. Zolki. *J. Am. Chem. Soc*. **75**, 6202 (1953).
31. (a) C. Cadena, Q. Zhao, R. Q. Snurr, E. J. Maginn. *J. Phys. Chem. B* **110**, 2821 (2006); (b) M. Lagache, P. Ungerer, A. Boutin, A. H. Fuchs. *Phys. Chem. Chem. Phys.* **3**, 4333 (2001).
32. L. V. Gurvich, I. V. Veyts, C. B. Alcock. *Thermodynamic Properties of Individual Substances*, 4th ed., Hemisphere Publishing, New York (1989).
33. (a) N. B. Wilding. *Phys. Rev. E* **52**, 602 (1995); (b) J. A. Zollweg, G. W. Mulholland. *J. Chem. Phys.* **57**, 1021 (1972).
34. (a) J. L. Haws, D. G. Harden. *J. Spacecr. Rockets* **2**, 972 (1965); (b) L. F. Audrieth, B. Ackerson-Ogg. *The Chemistry of Hydrazine*, John Wiley, New York (1951).
35. (a) A. M. Ferrenberg, R. H. Swendsen. *Phys. Rev. Lett*. **61**, 2635 (1988); (b) A. M. Ferrenberg, R. H. Swendsen. *Phys. Rev. Lett*. **63**, 1195 (1989).
36. O. A. Knight. *Hydrocarbon Proc. Petr. Refiner.* **41**, 179 (1962).
37. D. Frenkel, B. Smit. *Understanding Molecular Simulation*, Academic Press, New York (1996).
38. F. Franks. *Water, A Matrix of Life*, 2nd ed., The Royal Society of Chemistry, Cambridge (2000).
39. W. Jiang, T. Yan, Y. Wang, G. A. Voth. *J. Phys. Chem. B* **112**, 3121 (2008).
40. D. A. McQuarrie. *Statistical Mechanics*, University Science Books, Sausalito, CA (2000).
41. R. P. W. J. Struis, J. de Bleijser, J. C. Leyte. *J. Phys. Chem.* **91**, 1639 (1987).
42. M. S. Kelkar, E. J. Maginn. *J. Chem. Phys.* **123**, 224904 (2005).
43. M. S. Grigoriev, P. Moisy, C. Den Auwer, I. A. Charushnikova. *Acta Crystallogr., Sect. E* **61**, i216 (2005).
44. O. de Bonn, A. Hammerl, T. M. Klapötke, P. Mayer, H. Piotrowski, H. Zewen. *Z. Anorg. Allg. Chem.* **627**, 2011 (2001).
45. T. Hawkins. "Research and Development of Ionic Liquids at U.S. Air Force Research Laboratory Ionic Liquids R&D – U.S. Air Force Research Laboratory" Project No. 5026, Task No. 0541, Air Force Research Laboratory, Edwards Air Force Base, CA (report date: April 2005).
46. S. J. Grabowski. *Annu. Rep. Prog. Chem., Sect. C* **102**, 131 (2006).
47. D. M. Eike, J. F. Brennecke, E. J. Maginn. *J. Chem. Phys*. **122**, 014115 (2005).
48. (a) T. Yan, C. J. Burnham, M. G. DelPopolo, G. A. Voth. *J. Phys. Chem. B* **108**, 11877 (2004); (b) B. L. Bhargava, S. Balasubramanian. *J. Chem. Phys.* **127**, 114510 (2007).